Soils and Foundations 2012;52(2):257–278

The Japanese Geotechnical Society

Soils and Foundations

www.sciencedirect.com
journal homepage: www.elsevier.com/locate/sandf

Seismic evaluation of soil–foundation–superstructure system considering geometry and material nonlinearities of both soils and structures

Yuanfeng Bao[a], Guanlin Ye[b], Bin Ye[c], Feng Zhang[a,*]

[a]*Department of Civil Engineering, Nagoya Institute of Technology, Showa-ku, Gokiso-cho, Nagoya 466-8555, Japan*
[b]*Department of Civil Engineering, Shanghai Jiaotong University, Dongchuan Road 800, Shanghai 200240, China*
[c]*Department of Geotechnical Engineering, Tongji University, Siping Road 1239, Shanghai 200092, China*

Available online 29 March 2012

Abstract

In this paper, in order to increase the accuracy of numerical simulations using finite element methods related to soil–structure interaction problems, the influence of the geometric and material nonlinearities of structures was carefully investigated. By introducing proper models dealing with the geometric and material nonlinearities of structures, the authors have proposed a numerical method for the modeling of the nonlinearity of soils that have been carefully investigated in past research, and also for the modeling of structures based on finite deformation schemes. The accuracy of the numerical analysis related to the structures was firstly verified with an Abaqus (2008) calculation. The calculation was conducted with a program named DBLEAVES (Ye, 2007, 2011). Furthermore, 2D soil–water coupled dynamic analyses, in the finite deformation schemes of both soils and structures, were conducted on a soil-group pile foundation–superstructure system to investigate the seismic behavior of an elevated bridge during a major earthquake, in which strong nonlinear behavior of geometry and material are expected for both the soils and the structures. The applicability of the proposed numerical method to soil–structure interaction problems encountered in many fields of geotechnical and structural engineering was carefully checked. The main purpose of the research is to propose a numerical method by which it is possible to describe the soil–structure interaction problems with a level of accuracy that can satisfy the needs of both the geotechnical and structural engineering fields.

Keywords: Finite deformation; Constitutive model; Dynamic FEM; Liquefaction; Soil–foundation–superstructure interaction (IGC: E-08, E-12)

1. Introduction

In the numerical analysis of geotechnical engineering, the material nonlinearity of soil usually needs to be considered. As a result, research on constitutive models of geomaterials have been extensively undertaken for many years by many researchers and great progress has been made in this field. Meanwhile, the finite deformation scheme in the finite element method (FEM) has also been well developed and some interesting results have been published in the literature. In addition, the geometric and material nonlinearities of structures have also been investigated intensively by researchers in structural engineering, with some of their programs now commercially available

*Corresponding author. Tel./fax: +81 52 735 7923.
E-mail address: cho.ho@nitech.ac.jp (F. Zhang).

Peer review under responsibility of The Japanese Geotechnical Society
doi:10.1016/j.sandf.2012.02.005

Nomenclature

γ	unit weight of materials
v	Poisson's ratio
e_0	initial void ratio
K_w	elastic volumetric stiffness of water
k	permeability of soil
λ	compression index of soil
κ	swelling index of soil
R_f	critical state parameter ($=\sigma_1/\sigma_3$)
OCR	overconsolidation ratio
R_0^*	reference degree of structure
ς_0	reference anisotropy
m	degradation parameter of overconsolidation state
m^*	degradation parameter of structure
b_r	evolution parameter of anisotropy
b_l	parameter for anisotropy, default = 0.95
E_c	Young's modulus of concrete
σ_c	compressive strength of concrete
σ_t	tensile strength of concrete
E_s, E_t	Young's modulus and tangent modulus of steel
σ_{y0}	initial yield strength of steel
A	area of cross section
I_x, I_y	secondary moment of inertia about x, y axis
J	torsional moment of inertia
$a1$, $a2$	the first and second reduced ratio for RC trilinear beam
M_c, M_y, M_u	cracking, yielding and failure moments for RC trilinear beam
t	thickness of thin-wall pier

and widely used in numerical analysis. In considering boundary value problems related to soil–structure interactions, both the structure and the soil are involved in the calculation. Therefore, it is important to properly consider the geometric and material nonlinearities of both the structures and the soils. Unfortunately, due to the different aims between geotechnical engineering and structural engineering, geotechnical engineers usually pay more attention to the soil properties than to the structures. Vise verse, structural engineers usually pay more attention to the structural properties than to the soils. As a result, in simulating the soil–structure interaction problems, sophisticated models describing the geometric and material nonlinearities are usually applied only to one aspect and the other aspect is neglected. Therefore, in order to increase the accuracy of numerical analysis for soil–structure interaction problems to a such a level that satisfies the requirements of both geotechnical and structural engineers, a numerical method needs to be developed in which the geometric and material nonlinearities of both the soils and the structures are properly modeled.

Due to quick developments in the research field of constitutive models for geomaterials and the finite deformation scheme in FEM, the accuracy of numerical analysis for soils with FEM has improved significantly, e.g., the works by Yashima et al. (1991), Oka (1992), Oka et al. (1992, 1994, 1999), Asaoka et al. (1994), Ye (2007), Ye et al. (2007), Noda et al. (2008), Xia et al. (2010), Jin et al. (2010a). In geotechnical engineering, however, it is known that not only the nonlinear behavior of the soils but also the superstructures and foundation structures like piles may greatly affect the accuracy of the numerical analysis. For instance, in simulating the dynamic behavior of a group-pile foundation subjected to earthquake vibration, a full system, which consists of superstructures, a group-pile foundation and a ground, is required for use in a dynamic FEM analysis (Zhang and Kimura, 2002). There is no doubt that a suitable constitutive model for soil is absolutely necessary (Zhang et al., 2000), while a proper model for describing the material nonlinearity of piles has also proved to be very important in the works by Zhang and Kimura (2002) and Jin et al. (2010b).

On the other hand, the nonlinear behaviors of the superstructure tend to be neglected by geotechnical engineers because of different interests between the researchers in the fields of geotechnical engineering and structural engineering. In most cases, the modeling of superstructures used in geotechnical engineering is so primitive that structural engineers would likely scoff at them. The models and schemes for the geometric and material nonlinearities of structures, however, have been developed for many years and are quite well-matured, e.g., the works by Hsiao et al. (1987), Goto et al. (1995), Li (1997), Wang (1997) and Li and Goto (1998). If these models and schemes are properly applied in geotechnical engineering, the accuracy of numerical analysis with FEM can be expected to significantly improve.

In this paper, a rigorous numerical scheme for a space beam element (Goto et al., 1995; Li, 1997) that can properly take the geometric and the material nonlinearities of structures into consideration, was introduced and embedded into the DBLEAVES (Ye, 2007, 2011). In order to check the accuracy and ability of the proposed method, an elastoplastic analysis of a thin-walled column, subjected to three directional loading and which had undergone extremely large deformation, was carried out and the results of the calculation were compared and checked with the existing results that can be found in the literature.

Furthermore, 2D soil–water coupled dynamic analyses, in the finite deformation schemes of both soils and structures, were conducted on a soil-group pile foundation–superstructure system to investigate the seismic behavior of an elevated bridge with a 12-pile foundation during a major earthquake, in which strong nonlinear behaviors of geometry and material are expected for both the soils and the structures. The applicability of the

proposed numerical method to soil–structure interaction problems that might be encountered in many fields of geotechnical engineering is carefully checked.

2. Nonlinear scheme of beam

2.1. Geometric nonlinear scheme of beam

In order to solve the geometric nonlinear problem, an incremental stiffness matrix is preferred. The main difficulty in inducing geometric nonlinearity into analysis, however, is due to the finite rotations in a fixed coordinate space that cannot be treated as vector quantities. A co-rotational procedure for handling the large rotations of beam structures was adopted in the works by Goto et al. (1995) and Li (1997) where no restrictions were needed for the magnitude of finite deformations in three-dimensional space. In this section, this procedure will be briefly presented.

Two coordinate systems shown in Fig. 1 are used to derive the element stiffness equation. One is the fixed rectangular Cartesian coordinate system (x, y, z), also known as the local member coordinate or member coordinate in abbreviation, with the base vectors (g_x, g_y, g_z) defined at the initial configuration of a beam element. The other is the orthogonal co-rotational coordinate system ($\overline{x},\overline{y},\overline{z}$) with the base vectors ($\overline{i}_x,\overline{i}_y,\overline{i}_z$) and the origin located at one end of the element. This coordinate system moves with the rigid body rotation of the beam element. The directions of ($\overline{x},\overline{y},\overline{z}$) coincide with the averaged directions of the two sets of the deformed base vectors ($\hat{g}_{xi},\hat{g}_{yi},\hat{g}_{zi}$), $(i=1,2)$ at Node1 and Node2.

Corresponding to the two coordinate systems, two sets of nodal forces and displacement components for a beam element are introduced respectively. One is expressed in terms of the fixed member coordinates (x, y, z) as

$$\{f_i\}=\{F_{x1},F_{y1},F_{z1},M_{x1},M_{y1},M_{z1},F_{x2},F_{y2},F_{z2},M_{x2},M_{y2},M_{z2}\}^T \quad (1)$$

$$\{d_i\}=\{u_1,v_1,w_1,\theta_{x1},\theta_{y1},\theta_{z1},u_2,v_2,w_2,\theta_{x2},\theta_{y2},\theta_{z2}\}^T \quad (2)$$

The other one is defined with respect to the moving coordinates ($\overline{x},\overline{y},\overline{z}$) as

$$\{\overline{f}_i\}=\{\overline{F}_{x1},\overline{F}_{y1},\overline{F}_{z1},\overline{M}_{x1},\overline{M}_{y1},\overline{M}_{z1},\overline{F}_{x2},\overline{F}_{y2},\overline{F}_{z2},\overline{M}_{x2},\overline{M}_{y2},\overline{M}_{z2}\}^T \quad (3)$$

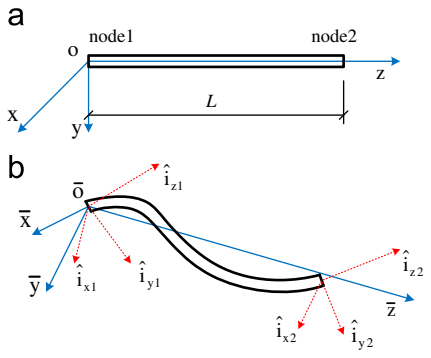

Fig. 1. Coordinate systems in co-rotational procedure. (a) Local member coordinate system and (b) moving co-rotational coordinate system.

$$\{\overline{d}_i\}=\{\overline{u}_1,\overline{v}_1,\overline{w}_1,\overline{\theta}_{x1},\overline{\theta}_{y1},\overline{\theta}_{z1},\overline{u}_2,\overline{v}_2,\overline{w}_2,\overline{\theta}_{x2},\overline{\theta}_{y2},\overline{\theta}_{z2}\}^T \quad (4)$$

Here, in order to realize the transformation of coordinates, Eulerian angles (φ_i,θ_i, ψ_i) $(i=1, 2)$ in terms of the fixed member coordinates (x, y, z) are introduced.

Then, with some manipulations, the relation of incremental displacements between the member coordinates (x, y, z) and the co-rotational coordinates ($\overline{x},\overline{y},\overline{z}$) is obtained as

$$\{\Delta\overline{d}_i\}=\left[\frac{\Delta\overline{d}_i}{\Delta d_j}\right]\{\Delta d_j\}=[R_{ij}]\{\Delta d_j\} \quad (i=1,6;j=1,12)$$

$$\{\Delta\overline{d}_i\}=\{\Delta\overline{u}_2,\Delta\overline{v}_2,\Delta\overline{w}_2,\Delta\overline{\theta}_{x2},\Delta\overline{\theta}_{y2},\Delta\overline{\theta}_{z2}\}^T;\quad \{\Delta d_j\}=\Delta\{d_j\} \quad (5)$$

where $[R_{ij}]$ is a 6×12 transformation matrix that is shown in detail in the appendix.

In the moving coordinate system, the rotational displacements are considered to be small under the assumption of small strains, if the rigid body rotations are removed. Based on the definition of the moving co-rotational coordinate system, the following equations hold:

$$\{\overline{u}_1,\overline{v}_1,\overline{w}_1\}=0 \quad (6)$$

$$\{\overline{\theta}_{x1},\overline{\theta}_{y1},\overline{\theta}_{z1}\}^T=-\{\overline{\theta}_{x2},\overline{\theta}_{y2},\overline{\theta}_{z2}\}^T \quad (7)$$

Therefore, the elastic stiffness equation in the moving coordinate system can be simplified as follows:

$$\begin{Bmatrix}\overline{F}_{x2}\\ \overline{F}_{y2}\\ \overline{F}_{z2}\\ \overline{M}_{x2}-\overline{M}_{x1}\\ \overline{M}_{y2}-\overline{M}_{y1}\\ \overline{M}_{z2}-\overline{M}_{z1}\end{Bmatrix}=\begin{bmatrix}12EI_y/l^3 & 0 & 0 & 0 & 0 & 0\\ 12EI_x/l^3 & 0 & 0 & 0 & 0 & \\ & & EA/l & 0 & 0 & 0\\ & & & 4EI_x/l & 0 & 0\\ & Sym & & & 4EI_y/l & 0\\ & & & & & 4GJ/l\end{bmatrix}\times\begin{Bmatrix}\overline{u}_2\\ \overline{v}_2\\ \overline{w}_2\\ \overline{\theta}_{x2}\\ \overline{\theta}_{y2}\\ \overline{\theta}_{z2}\end{Bmatrix} \quad (8)$$

or,

$$\{\overline{f}_i\}=[\overline{k}_{ij}]\{\overline{d}_i\}\quad (i=1,6;j=1,6) \quad (9)$$

based on the small displacement theory.

With the help of principle of virtual work, the following relation holds

$$\{f_j\}^T\{\Delta d_j\} = \{\overline{f}_i\}^T\{\Delta \overline{d}_i\} \quad (i=1,6; j=1,12) \tag{10}$$

Substituting Eq. (5) into Eq. (10) leads to

$$\{f_j\} = \left[\frac{\partial \overline{d}_i}{\partial d_j}\right]\{\overline{f}_i\} \quad (i=1,6;\ j=1,12) \tag{11}$$

Taking the total differential of $\{f_j\}$ leads to

$$\{\Delta f_j\} = \left[\frac{\partial \overline{d}_i}{\partial d_j}\right]^T\{\Delta \overline{f}_i\} + \left[\frac{\partial^2 \overline{d}_i}{\partial d_j \partial d_k}\Delta d_k\right]^T\{\overline{f}_i\}.$$
$$(i=1,6;\ j=1,12;\ k=1,12) \tag{12}$$

Because $[\overline{k}_{ij}]$ is constant, the incremental stiffness equation for a beam element in the co-rotational coordinates is expressed as

$$\{\Delta \overline{f}_i\} = [\overline{k}_{ij}]\{\Delta \overline{d}_j\} \quad (i=1,6;\ j=1,6) \tag{13}$$

Substituting Eqs. (5) and (13) into Eq. (12) finally yields an incremental stiffness equation expressed in terms of the coordinate systems (x, y, z) as

$$\{\Delta f_j\} = \left[[R]^T[\overline{k}][R] + \frac{\partial [R_{im}]^T}{\partial d_m}\{\overline{f}_i\}\right]\{\Delta d_j\} = [\Delta k]\{\Delta d_j\},$$
$$(i=1,6;\ j=1,12;\ m=1,12) \tag{14}$$

where $[\Delta k]$ is a 12×12 symmetric matrix, which will improve the efficiency of a nonlinear analysis. The transformation of the coordinates from the member coordinates to the global coordinates fixed in space is same as that of the usual finite element method.

In order to show the accuracy of the presented method and the program, a classical example firstly mentioned by Simo and Vu-Quoc (1986) is tested subsequently. The initially-straight cantilever, as shown in Fig. 2, is subjected to an end moment of

$$M^* = \frac{M\cdot L}{2\pi\cdot E\cdot I} = 1.0 \tag{15}$$

by which the beam is curled into a complete circle. In this example, following Li (1997), five elements are used in the calculation. The result is exactly the same as that of Li (1997). It should be noted here that, in the work by Li (1997), a Newton–Raphson iterative procedure was employed to solve the nonlinear overall stiffness equations. In the present paper, however, the incremental method is adopted.

2.2. Material nonlinear scheme of beam

For metal material, the elastoplastic constitutive law used in the present paper is based on the Von Mises yield criterion, the associated flow rule and a mixed strain hardening rule as shown in Figs. 3 and 4.

according to the mixed Von Mises yield criterion, the yield surface equation can be expressed as

$$f = g(\sigma_i-\alpha_i) = \sqrt{(\sigma_x-\alpha_x)^2+(\sigma_y-\alpha_y)^2+(\sigma_z-\alpha_z)^2+3(\tau_{xy}-\alpha_{xy})^2+3(\tau_{yz}-\alpha_{yz})^2+3(\tau_{zx}-\alpha_{zx})^2},\ (i=1,6) \tag{16}$$

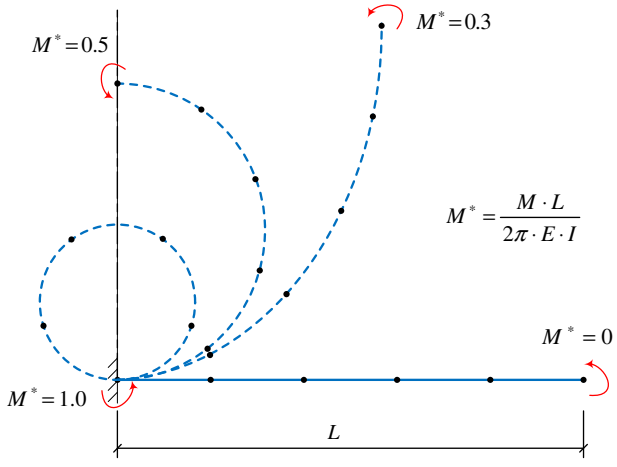

Fig. 2. Simulation of deformed geometries for cantilever subjected to an end-moment (beam material is elastic but geometry is nonlinear; calculated results are the same as those reported in the work by Li, 1997).

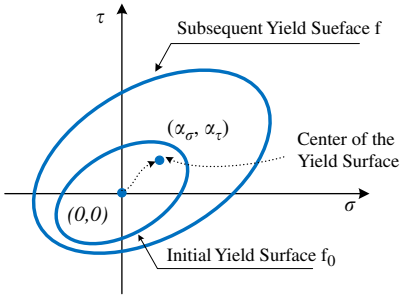

Fig. 3. Initial and subsequent yield surface.

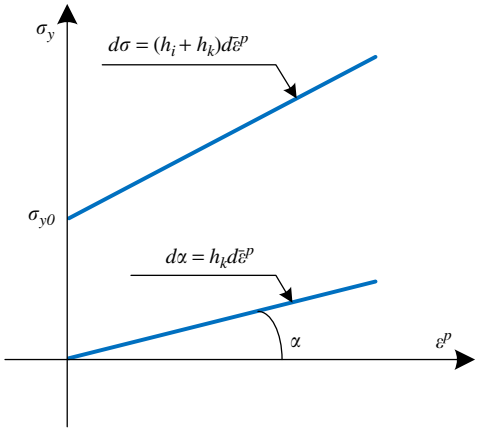

Fig. 4. One-dimensional illustration of mixed strain hardening rule.

where α_i is a back stress vector, a kinematic shift of the center for the yield surface as shown in Fig. 3. In the elastic state, stress–strain relationship has the following form:

$$\{d\sigma_i\}=[D]\{d\varepsilon_i^e\} \quad (i=1,6) \tag{17}$$

where $[D]$ is the elastic matrix. In the plastic deformation, total strain increments can be decomposed into two parts as

$$\{d\varepsilon_i\}=\{d\varepsilon_i^e\}+\{d\varepsilon_i^p\} \quad (i=1,6) \tag{18}$$

And since $d\varepsilon=d\sigma/E^t$, $d\varepsilon^e=d\sigma/E$, $d\varepsilon^p=d\sigma/E^p$, where E, E^t, E^p are Young's elastic, the tangent and the plastic modulus respectively, from Eq. (18) one has

$$E^p=\frac{E^t}{1-E^t/E} \tag{19}$$

According to the associated flow rule, from Eq. (16), we have

$$\{d\varepsilon_i^p\}=d\lambda\{\partial f/\partial\sigma_i\} \quad (i=1,6) \tag{20}$$

The differentiation of Eq. (16) yields

$$df=\frac{\partial f}{\partial\sigma_i}d\sigma_i+\frac{\partial f}{\partial\alpha_i}d\alpha_i \quad (i=1,6) \tag{21}$$

Further, the following relation holds:

$$\frac{\partial f}{\partial\sigma_i}=-\frac{\partial f}{\partial\alpha_i} \quad (i=1,6) \tag{22}$$

Substituting Eq. (22) into Eq. (21) yields

$$df=\frac{\partial f}{\partial\sigma_i}d\sigma_i-\frac{\partial f}{\partial\sigma_i}d\alpha_i \quad (i=1,6) \tag{23}$$

Based on the hypothesis of mixed hardening, it holds

$$df=h_{iso}d\bar{\varepsilon}^p; \quad \frac{\partial f}{\partial\sigma_i}d\alpha_i=h_{kin}d\bar{\varepsilon}^p \quad (i=1,6) \tag{24}$$

where h_{iso}, h_{kin} are the isotropic hardening and kinematic hardening coefficients, respectively, and

$$E^p=h_{iso}+h_{kin} \tag{25}$$

$\bar{\varepsilon}^p$ is the equivalent plastic strain expressed as follows:

$$\bar{\varepsilon}^p=\int d\bar{\varepsilon}^p \tag{26}$$

By using the virtual work principle, one has

$$(\sigma_i-\alpha_i)\cdot d\varepsilon_i^p=f\cdot d\bar{\varepsilon}^p \quad (i=1,6) \tag{27}$$

By substituting Eq. (20) into Eq. (27) and noticing the fact that $(\sigma_i-\alpha_i)\partial f/\partial\sigma_i=f(i=1,6)$, one has

$$d\lambda=d\bar{\varepsilon}^p \tag{28}$$

From Eq. (24), one has

$$(h_{iso}+h_{kin})d\bar{\varepsilon}^p=df+\left(\frac{\partial f}{\partial\sigma_i}d\alpha_i\right) \quad (i=1,6) \tag{29}$$

Substitution of Eqs. (20) and (23) into Eq. (29) yields

$$\begin{aligned}(h_{iso}+h_{kin})d\bar{\varepsilon}^p&=\frac{\partial f}{\partial\sigma_i}d\sigma_i=\frac{\partial f}{\partial\sigma_i}[D]\{d\varepsilon_i-d\varepsilon_i^p\}\\&=\frac{\partial f}{\partial\sigma_i}[D]\left\{d\varepsilon_i-d\bar{\varepsilon}^p\frac{\partial f}{\partial\sigma_i}\right\}, \quad (i=1,6)\end{aligned} \tag{30}$$

From Eq. (30), one has

$$d\lambda=d\bar{\varepsilon}^p=\frac{\{\partial f/\partial\sigma_i\}^T[D]}{E^p+\{\partial f/\partial\sigma_j\}^T[D]\{\partial f/\partial\sigma_j\}}\{d\varepsilon_i\} \quad (i=1,6;\ j=1,6) \tag{31}$$

Since the stress increments are only related to the elastic strain increments, the following relation holds:

$$\{d\sigma_i\}=[D][\{d\varepsilon_i\}-\{d\varepsilon_i^p\}]=[D][\{d\varepsilon_i\}-d\bar{\varepsilon}^p\{\partial f/\partial\sigma_i\}] \quad (i=1,6) \tag{32}$$

Finally, by substituting Eq. (31) into Eq. (32), the incremental elastoplastic stress–strain relationship can be obtained as follows:

$$\begin{aligned}\{d\sigma_i\}&=\left([D]-\frac{[D]\{\partial f/\partial\sigma_j\}\{\partial f/\partial\sigma_j\}^T[D]}{E^p+\{\partial f/\partial\sigma_k\}^T[D]\{\partial f/\partial\sigma_k\}}\right)\{d\varepsilon_i\}\\&=[D_{ep}]\{d\varepsilon_i\}, \quad \left\{\begin{matrix}i=1,6\\j=1,6\\k=1,6\end{matrix}\right\}\end{aligned} \tag{33}$$

where $[D_{ep}]$ is the elastoplastic matrix.

According to Ziegler's modification of Prager's model, the evolution of the back stress tensor, which defining the subsequent yield surface, can be expressed as follows:

$$\{d\alpha_i\}=d\mu\{\sigma_i-\alpha_i\} \quad (i=1,6) \tag{34}$$

By substituting Eq. (34) into Eq. (24) and noticing the fact that $(\sigma_i-\alpha_i)\partial f/\partial\sigma_i=f$ $(i=1,6)$, we have

$$d\mu=\frac{h_{kin}d\bar{\varepsilon}^p}{f} \tag{35}$$

and

$$\{d\alpha_i\}=\frac{h_{kin}((\partial f/\partial\sigma_j)d\sigma_j)}{(h_{iso}+h_{kin})f}\{\sigma_i-\alpha_i\} \quad (i=1,6;\ j=1,6) \tag{36}$$

In order to check the validity of the presented constitutive law, an example of a mixed strain hardening bilinear model is subsequently simulated. For simplicity, the stress vector consists of only two components, the normal and the shear stresses. The values of the material parameters and loading condition in the calculation are shown in Table 1. In Fig. 5, the results for the isotropic hardening, the mixed hardening and the kinematic hardening are shown, respectively. Though return mapping methods, which can draw the stresses back to the yield surface

Table 1
Material parameters of steel and loading condition.

E_s	2.1×10^5 MPa	Young's modulus
E^t	2.1×10^4 MPa	The tangent modulus
v	0.25	Poisson ratio
σ_{y0}	360 MPa	Initial yield strength
	1.0	Isotropic hardening
h_m	0.60	Mixed hardening
	0.00	Kinematic hardening
ε	–0.005–0.005	Proportional loading in two
γ	–0.003–0.003	directions by strain control

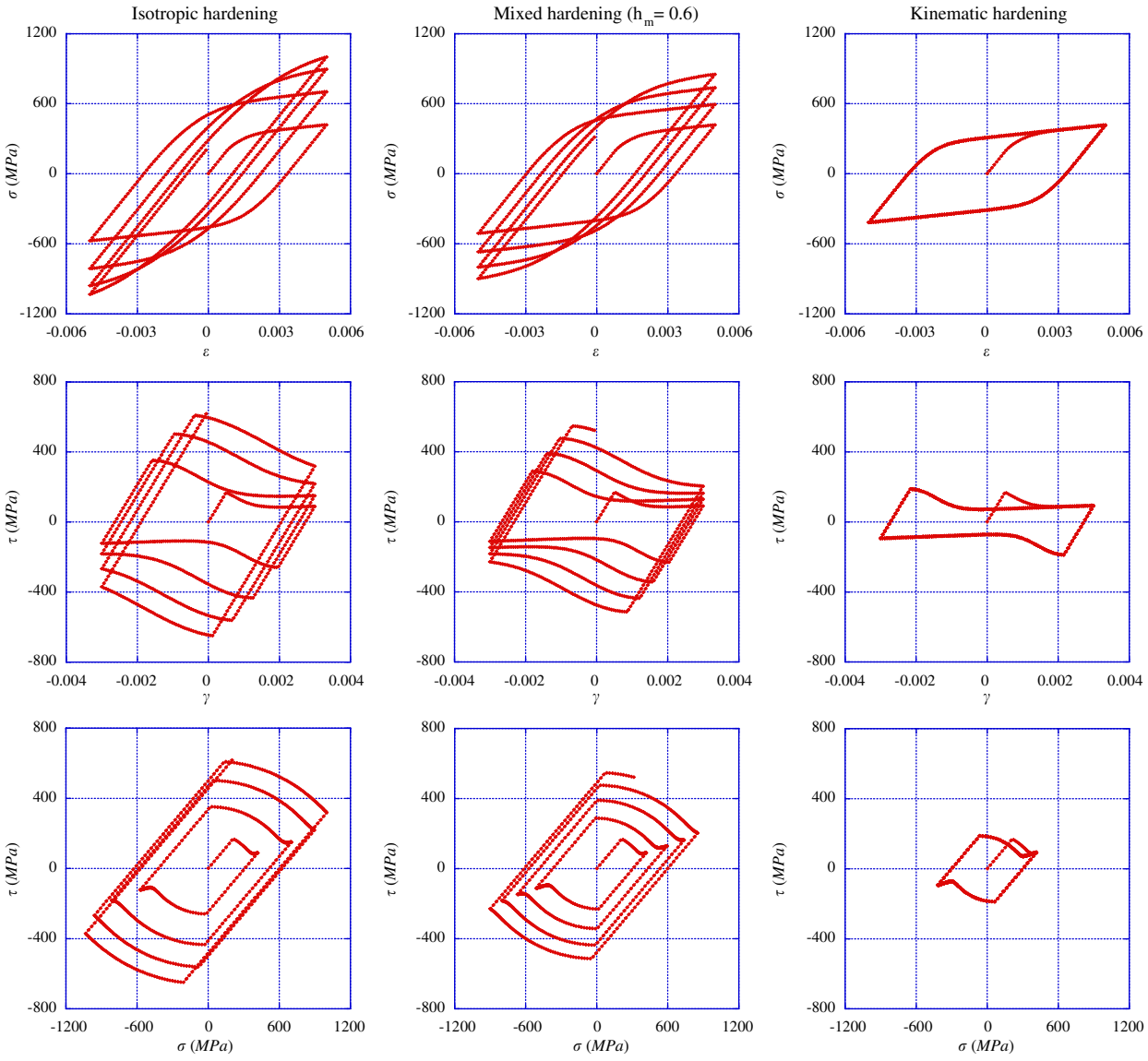

Fig. 5. Stress–strain relation and stress path in different strain hardening rule (bilinear model).

(Li and Goto, 1998), are not employed in the present calculation, the calculated results are quite good because the incremental loading of each step in calculating the nonlinear equations is small enough to ensure satisfactory accuracy.

2.3. Beam element with thin-walled cross-section

Thin-wall shaped cross section is very common in steel structural members in which the thickness of the wall is much smaller than those of the span length. Based on the preceding description, a finite deformation scheme for space-beam element with thin-walled members in *closed section* or *open section* was established when the effect of warping deformation is not comparable with those of bending and axial deformations, as shown in Fig. 6. In order to consider the effect of transverse shear deformation due to bending, a Timoshenko beam element is used for the analysis of finite element in the co-rotational coordinate system $(\overline{x},\overline{y},\overline{z})$. The basic assumptions are the following:

(1) The cross section is thin-walled bi-axial symmetric.
(2) The strains are infinitesimal, although the rotations and displacements may be finite.
(3) It is not necessary for the plane normal to the beam axis before deformation to be perpendicular to the axis after deformation but to remain a plane.

According to the assumptions (2) and (3), the rotation angles around $\overline{x}$ and $\overline{y}$ axes in the moving coordinates can be expressed as

$$\overline{\theta}_y = \overline{u}_{,z} - \gamma^b_{xz}; \quad \overline{\theta}_x = \overline{v}_{,z} - \gamma^b_{yz} \tag{37}$$

where γ^b_{xz} and γ^b_{yz} are the shear strains due to the transverse shear deformation. The axial displacement, rotations and

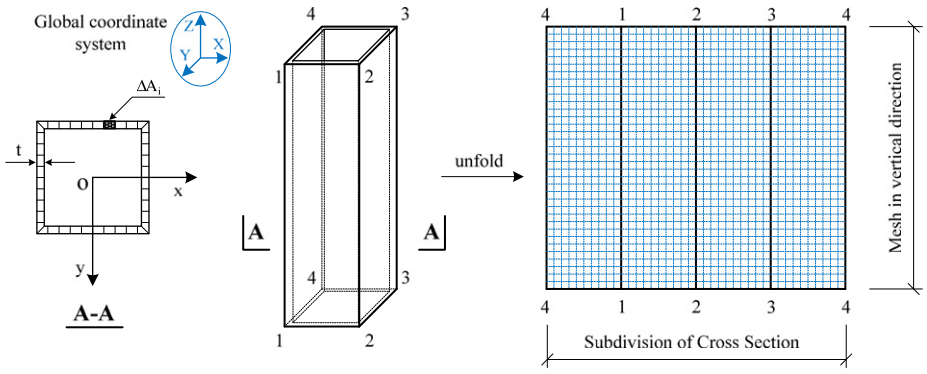

Fig. 6. Thin-walled beam element.

transverse displacements are assumed to be linear and quadratic polynomials, respectively

$$\overline{w} = a_0 + a_1\overline{z}; \quad \overline{u} = b_0 + b_1\overline{z} + b_2\overline{z}^2; \quad \overline{v} = c_0 + c_1\overline{z} + c_2\overline{z}^2$$
$$\overline{\theta}_z = d_0 + d_1\overline{z}; \quad -\overline{\theta}_x = e_0 + e_1\overline{z}; \quad \overline{\theta}_y = f_0 + f_1\overline{z}. \tag{38}$$

With the assumption that shear strains are constants along the element length, the constants in the displacement interpolate functions can be determined and expressed as follows:

$$\begin{aligned}
&\overline{w} = N_1\overline{w}_1 + N_2\overline{w}_2\\
&\overline{u} = N_1\overline{u}_1 + N_3\overline{\theta}_{y1} + N_2\overline{u}_2 - N_3\overline{\theta}_{y2}\\
&\overline{v} = N_1\overline{v}_1 + N_3\overline{\theta}_{x1} + N_2\overline{v}_2 - N_3\overline{\theta}_{x2}\\
&\overline{\theta}_z = N_1\overline{\theta}_{z1} + N_2\overline{\theta}_{z2}\\
&-\overline{\theta}_x = -N_1\overline{\theta}_{x1} - N_2\overline{\theta}_{x2}\\
&\overline{\theta}_y = N_1\overline{\theta}_{y1} + N_2\overline{\theta}_{y2}
\end{aligned} \tag{39}$$

where

$$N_1 = 1 - \overline{z}/l; \quad N_2 = \overline{z}/l; \quad N_3 = \overline{z}/2(1 - \overline{z}/l) \tag{40}$$

are the shape functions. Thus, the normal strain and shear strain of a finite element can be given as

$$\begin{aligned}
&\varepsilon_z = \overline{w}_{,z} - \overline{x}\overline{\theta}_{y,z} - \overline{y}\overline{\theta}_{x,z} = [N_\varepsilon]\{\overline{d}\}\\
&\gamma_{xz} = \gamma^s_{xz} + \gamma^b_{xz} = \overline{u}_{,z} - \overline{\theta}_y + \Theta_y\overline{\theta}_{z,z} = [N_{xz}]\{\overline{d}\}\\
&\gamma_{yz} = \gamma^s_{yz} + \gamma^b_{yz} = \overline{v}_{,z} - \overline{\theta}_x + \Theta_x\overline{\theta}_{z,z} = [N_{yz}]\{\overline{d}\}
\end{aligned} \tag{41}$$

where

$$\begin{aligned}
&[N_\varepsilon] = [0, 0, -1/l; -\overline{y}/l, -\overline{x}/l, 0; 0, 0, 1/l; \overline{y}/l, -\overline{x}/l, 0]\\
&[N_{xz}] = [-1/l, 0, 0; 0, -1/2, -\Theta_y/l; 1/l, 0, 0; 0, -1/2, \Theta_y/l]\\
&[N_{yz}] = [0, -1/l, 0; 1/2, 0, -\Theta_x/l; 0, 1/l, 0; 1/2, 0, \Theta_x/l]
\end{aligned} \tag{42}$$

and

$$\Theta = \begin{cases} 2n & open-section \\ 2n - \dfrac{\oint h^*_n ds}{t\oint (1/t) ds} & closed-section \end{cases} \tag{43}$$

As shown in Fig. 7, n is the normal distance from the centerline of the thin wall and t is the thickness of the wall. h^*_n is the distance from the shear center to the centerline. From Eq. (41), it is known that the total shear strain consists of transverse shear deformation and torsional

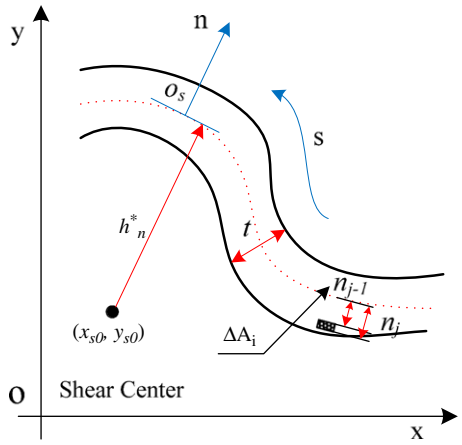

Fig. 7. Initial and subsequent yield surface (Goto et al., 1995).

shear deformation. The increments of the strains and the increments of stresses can be obtained as follows:

$$\Delta\varepsilon_z = [N_\varepsilon]\{\Delta\overline{d}\}; \quad \gamma_{xz} = [N_{xz}]\{\Delta\overline{d}\}; \quad \gamma_{yz} = [N_{yz}]\{\Delta\overline{d}\} \tag{44}$$

For thin-walled members, only the shear strain and stress along s-direction are combined with the normal strain and stress, while the shear strain and stress that are perpendicular to s-direction are neglected. Therefore, in the present study the elasto-plastic relationship of incremental stresses and incremental strains in the moving co-rotational coordinate system can be expressed as

$$\begin{Bmatrix} \Delta\sigma \\ \Delta\tau \end{Bmatrix} = [D_{ep}]\begin{bmatrix} [N_\varepsilon] \\ [N_\gamma] \end{bmatrix}\{\Delta\overline{d}\} \tag{45}$$

Using the principle of virtual work and assuming the absence of distributed loads, the stiffness equation of an element in the moving coordinates can be derived as follows:

$$\int_v \delta\{\varepsilon\}^T\{\sigma\}dv - \delta\{\overline{d}\}^T\{\overline{f}^e\} = 0 \tag{46}$$

Substituting Eqs. (44) and (45) into Eq. (46) yields

$$\int_v \delta\{\Delta d\}^T\{[N_\varepsilon]^T[N_\gamma]^T\}[D_{ep}]\begin{Bmatrix} [N_\varepsilon] \\ [N_\gamma] \end{Bmatrix}dv - \delta\{\Delta\overline{d}\}^T\{\Delta\overline{f}^e\} = 0 \tag{47}$$

By considering Eqs. (6) and (7), the elastoplastic tangential stiffness matrix can be obtained as follows:

$$[\Delta\bar{k}] = \begin{bmatrix} D_{22}\frac{A}{l} & 0 & D_{12}\frac{A}{l} & 2D_{12}\frac{S_y}{l} & -2D_{12}\frac{S_x}{l} & 2D_{22}\frac{I_{ry}}{l} \\ & 0 & 0 & 0 & 0 & 0 \\ & & D_{11}\frac{A}{l} & 2D_{11}\frac{S_y}{l} & -2D_{11}\frac{S_x}{l} & 2D_{12}\frac{I_{ry}}{l} \\ & & & 4D_{11}\frac{I_x}{l} & -4D_{11}\frac{S_{xy}}{l} & 4D_{12}\frac{I_{ryy}}{l} \\ & Sym. & & & 4D_{11}\frac{I_y}{l} & -4D_{12}\frac{I_{rxy}}{l} \\ & & & & & 4D_{22}\frac{J_x}{l} \end{bmatrix} \tag{48}$$

if the coordinate axis x is in s-direction and

$$[\Delta\bar{k}] = \begin{bmatrix} 0 & 0 & 0 & 0 & 0 & 0 \\ & D_{22}\frac{A}{l} & D_{12}\frac{A}{l} & 2D_{12}\frac{S_y}{l} & -2D_{12}\frac{S_x}{l} & 2D_{22}\frac{I_{rx}}{l} \\ & & D_{11}\frac{A}{l} & 2D_{11}\frac{S_y}{l} & -2D_{11}\frac{S_x}{l} & 2D_{12}\frac{I_{rx}}{l} \\ & & & 4D_{11}\frac{I_x}{l} & -4D_{11}\frac{S_{xy}}{l} & 4D_{12}\frac{I_{ryx}}{l} \\ & Sym. & & & 4D_{11}\frac{I_y}{l} & -4D_{12}\frac{I_{rxx}}{l} \\ & & & & & 4D_{22}\frac{J_y}{l} \end{bmatrix} \tag{49}$$

if the coordinate axis y is in s-direction. Here, D_{ij} are the components of the elastoplastic matrix $[D_{ep}]$, and

$$S_x = \sum_{i=1}^{m} x_i \Delta A_i; \quad S_y = \sum_{i=1}^{m} y_i \Delta A_i; \quad S_{xy} = \sum_{i=1}^{m} x_i y_i \Delta A_i$$

$$I_x = \sum_{i=1}^{m} y_i^2 \Delta A_i; \quad I_y = \sum_{i=1}^{m} x_i^2 \Delta A_i$$

$$I_{rx} = \sum_{i=1}^{m} \Theta_{xi} \Delta A_i; \quad I_{ry} = \sum_{i=1}^{m} \Theta_{yi} \Delta A_i$$

$$I_{rxy} = \sum_{i=1}^{m} x_i \Theta_{yi} \Delta A_i; \quad I_{ryx} = \sum_{i=1}^{m} y_i \Theta_{xi} \Delta A_i$$

$$I_{rxx} = \sum_{i=1}^{m} x_i \Theta_{xi} \Delta A_i; \quad I_{ryy} = \sum_{i=1}^{m} y_i \Theta_{yi} \Delta A_i$$

$$J_x = \sum_{i=1}^{m} \Theta_{yi}^2 \Delta A_i; \quad J_y = \sum_{i=1}^{m} \Theta_{xi}^2 \Delta A_i \tag{50}$$

where, m is the number of divided segments and ΔA_i is the area of the segment i. The derivation of Eqs. (48) and (49) is based on the fact that both the normal and the shear strains are constants along the length of the element so that the numerical integration can be avoided in Eq. (47). As shown in Fig. 6, the cross sectional area of the beam element is divided into m segmental areas in order to consider the individual plastic behavior of each segment, following the customary procedures of the plastic zone method (Li and Goto, 1998). Therefore, the beam element will be discretized into small finite elements along the axial direction, and the cross section of the member will be subdivided into a necessary number of segments, depending on the required accuracy.

Correspondingly, the internal moments, shear forces and axial force can be summed to

$$\overline{F}_{x2} = \sum_{i=1}^{m} (\tau_{xz})_i \Delta A_i; \quad \overline{F}_{y2} = \sum_{i=1}^{m} (\tau_{yz})_i \Delta A_i; \quad \overline{F}_{z2} = \sum_{i=1}^{m} \sigma_i \Delta A_i$$

$$\overline{M}_{x2} - \overline{M}_{x1} = 2\sum_{i=1}^{m} \sigma_i y_i \Delta A_i; \quad \overline{M}_{y2} - \overline{M}_{y1} = -2\sum_{i=1}^{m} \sigma_i x_i \Delta A_i$$

$$\overline{M}_{z2} - \overline{M}_{z1} = -2\sum_{i=1}^{m} \tau_i \Theta_i \Delta A_i \tag{51}$$

Finally, by substituting the elastic stiffness matrix $[\bar{k}]$ in Eq. (14) with the elastoplastic ones expressed in Eqs. (48) and (49), the elastoplastic tangential stiffness matrix in terms of the member coordinate system can be obtained.

The presented thin-walled beam element is embedded into the DBLEAVES. In order to check the accuracy and ability to deal with the extremely large rotations of the described method, an elastoplastic analysis of a thin-walled column subjected to three directional loading was carried out, as shown in Fig. 8. All of the free degrees at the column bottom end are restricted. The values of the material parameters and the loading condition in the simulation are shown in Table 2. In the calculation, the loading condition is force-controlled proportional loading in three directions, that is, the forces F_X, F_Y and F_Z are proportionally loaded simultaneously, as shown in Fig. 8.

Fig. 9 shows the calculated results and their comparison with the results obtained from the Abaqus (2008) calculation. In the figure, all the horizontal axes of the graphs represent the loading ratio, which is a ratio between the current force and the maximum force.

Fig. 9(a–c) shows the results of the displacements at the top of the column in three directions, respectively. Except for the displacement along the y direction, the results from both calculations coincide well with each other. In the y direction, because of its subordinate condition (the load in the x direction is much larger than that of the y direction), the discrepancy is a little bit large.

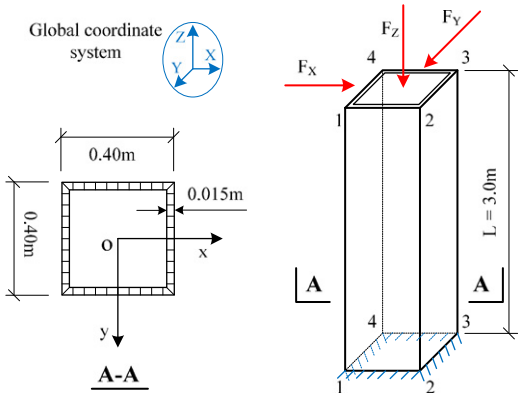

Fig. 8. Column subjected to three directional loadings.

Fig. 9(d–f) shows the results of the sectional forces S_x, S_y and N_z. It is known from these figures that the external forces are completely the same as the internal forces, that is, the sectional forces, showing that the accuracy of the calculation with the present method is very high.

Table 2
Material parameters of steel and loading condition.

E_s	2.1×10^5 MPa	Young's modulus
E^t	2.1×10^4 MPa	The tangent modulus
v	0.25	Poisson ratio
σ_{y0}	360 MPa	Initial yield strength
h_m	1.0	Isotropic hardening
m	100	Segments' number
n	20	Mesh number
F_X	5000.0 kN	Loading in X direction
F_Y	3000.0 kN	Loading in Y direction
F_Z	–1500.0 kN	Loading in Z direction
Step	10,000	Incremental steps number

Fig. 9(g–i) shows the results of the two bending moments M_x, M_y and the torsional moment T_z, at the bottom of the column, respectively. In the figures, three curves are plotted for comparison purposes. The third line, marked by distinct dots, represents the moments calculated directly from the external force and its acting position that has been deformed significantly, and are called FD-based calculations for simplicity. The other two lines represent the internal forces calculated with Abaqus and DBLEAVES. The good agreement clear in the figures indicates that both the nonlinearity of geometry and material can be described simultaneously and with high accuracy.

It should be pointed out that the theoretic reasoning about the nonlinear scheme of beams discussed in this chapter is the work of Goto et al. (1995) and Li (1997).

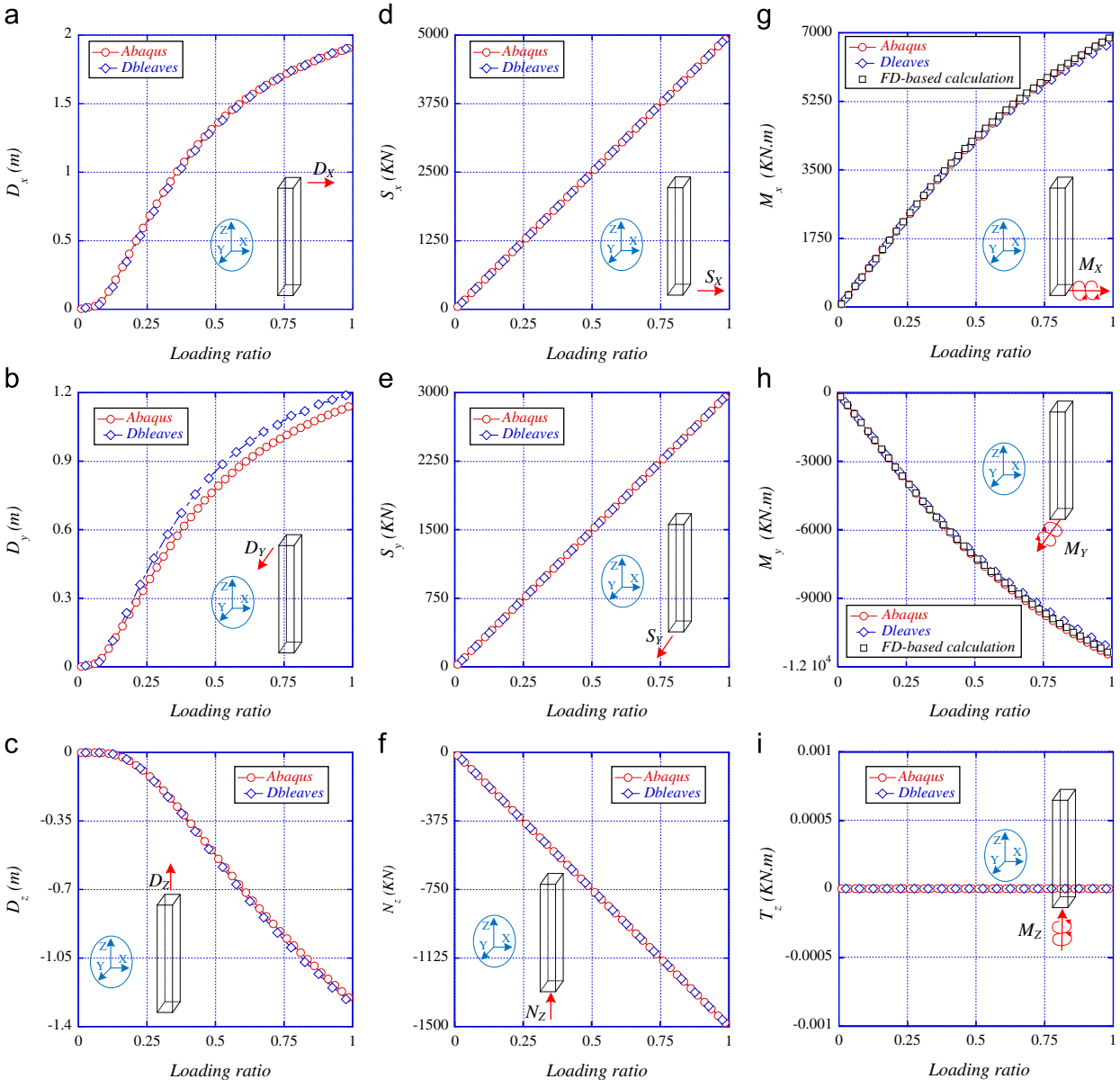

Fig. 9. Results of a column subjected to three directional loadings.

What has been done in this paper is to introduce the scheme into DBLEAVES so that it is possible for geotechnical engineer to calculate superstructures more accurately.

3. Soil–water coupling dynamic analyses for soil–structure interaction problem in an elevated bridge during a huge earthquake

In this paper, a soil–water coupling finite difference–finite element (FD-FE) dynamic analyses was conducted to evaluate the seismic behavior of soil–structure interaction problem in an elevated bridge during a huge earthquake. In the analysis, the material nonlinearity of soils is described by a model named the cyclic mobility model (Zhang et al., 2007). In the model, some important concepts related to the mechanical behavior of soil, such as stress-induced anisotropy (Sekiguchi, 1977), subloading yield surface (Hashiguchi and Ueno, 1977), superloading yield surface (Asaoka et al., 1998) and transformed stress concept (Yao et al., 2008) were adopted and their intimate relationships were considered in a unified way for the first time. The model is capable of properly taking the influence of the stress-induced anisotropy, the density, the structure of soil and the intermediate stress into consideration. It can describe the mechanical behavior of soft soil subjected to different loadings, monotonic or cyclic, under different drainage conditions, drained or undrained, in a unified way with only eight fixed parameters. A detailed description of the model can be found in the work by Zhang et al. (2007, 2010, 2011). Evidence of successful applications of the model to the boundary value problem (BVP) of the soil–water coupling analysis in geotechnical engineering can be found in the work by Ye (2007), Ye et al. (2007), Xia et al. (2010) and Jin et al. (2010a,b).

In this analysis, a full system shown in Fig. 10 was modeled: it consisted of ground, a group RC-pile foundation and a steel box thin-walled pier as the superstructure for an elevated bridge. Because the bridge is near a river, a RC caisson was used to enhance the bank of the river.

The ground was composed of four layers. From surface to bottom, they were reclaimed sand, alluvial sand, alluvial clay and diluvial gravel, respectively. The top three layers of soils were described by the aforementioned cyclic mobility model and the Jaumann rate strain tensor was used in the cyclic mobility model to deal with the finite deformation of the soils. The corresponding values of the parameter of the cyclic mobility model and physical properties of the soils are listed in Tables 3 and 4. The pile group was laid on the fourth layer, which was supposed to be an elastic material in the numerical analysis. The RC caisson was expected to be the elastic material in the simulation, with material parameters as listed in Table 5.

The bridge was supported by a group-pile foundation made of 3×4 cast-in-place RC piles. The piles were 1.2 m in diameter (D) and 28.5 m in length, and the distance between the centers of two piles was $2.5D$, as shown in Fig. 11. In the analysis, the piles were modeled with an AFD model (Zhang and Kimura, 2002), which can describe the axial-force dependent behavior of the RC piles. In order to reduce the scale of calculation and focus on the behavior of soil–structure interaction, a plane strain model along the transverse direction of the foundation was

Table 3
Material parameters of cyclic mobility models for soils.

Soil	R_f	ν	e_0	λ	κ	m	m^*	b_r
Layer1	2.5	0.30	0.90	0.022	0.0080	0.10	2.5	1.5
Layer2	2.5	0.30	0.90	0.028	0.010	0.10	2.5	1.5
Layer3	2.5	0.40	0.88	0.0080	0.0020	1.1	0.020	0.50

Table 4
Physical properties and initial state of soils.

Soil	OCR	R_0^*	ς_0	γ (kN/m^3)	K_w (kPa)	k (m/s)
Layer1	2.0	0.75	0.00	18	2.2e6	1.0$e-$4
Layer2	2.0	0.75	0.00	18	2.2e6	1.0$e-$4
Layer3	2.0	0.75	0.00	17	2.2e6	1.0$e-$9

Table 5
Material parameters of elastic model for RC caisson.

E_c (kPa)	ν	γ (kN/m^3)
2.0e7	0.20	25

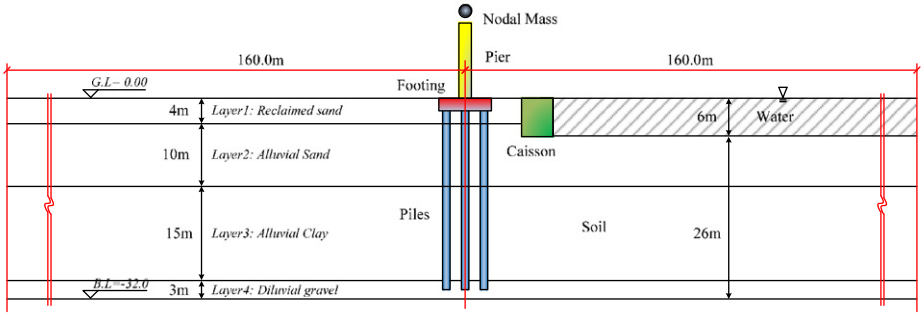

Fig. 10. Analysis model of the full system.

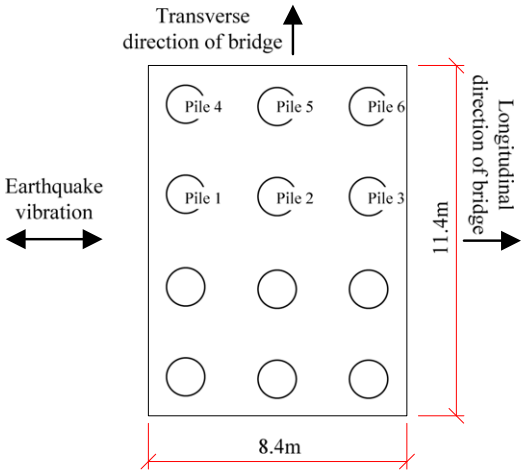

Fig. 11. Plane view of piles and footing.

Table 6
Material parameters of AFD model for piles (transformed value).

Compressive strength of concrete: σ_c=3.8*e*4 kPa (1.33*e*4 kPa)
Tensile strength of concrete: σ_t=3.0*e*3 kPa (1.05*e*3 kPa)
Young's modulus of concrete: E_c=3.0*e*7 kPa (1.05*e*7 kPa)
Yielding strength of steel: σ_{y0}=3.0*e*5 kPa (1.05*e*5 kPa)
Young's modulus of steel: E_s=2.1*e*8 kPa (7.37*e*7 kPa)
Arrangement of the reinforcement
main:ϕ29 × 28, hoop: ϕ16@300, OB (overburden of RC): 15 cm

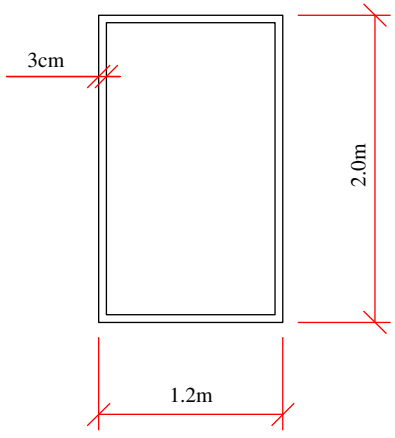

Fig. 12. Cross section of pier with thin-wall box.

schemed out. Therefore, the material parameters of the piles needed to be transformed for the plane strain problem according to equivalent stiffness, and the transformed parameters are listed in Table 6.

The pier has a rectangular cross section of 1.2 × 2.0 m^2 with a thickness of 3 cm and a height of 12.0 m, as shown in Fig. 12. A nodal mass of 1200 ton, representing the mass of the girder, and is located on the top of the pier. The parameters of the pier and the nodal mass should also be transformed to the plane strain problem according to equivalent stiffness, and the material parameters for the pier are listed in Tables 7–9.

The finite element mesh of the full system is shown in Fig. 13. The boundary condition of the ground was such that: (a) the bottom of the ground is fixed; (b) for the two side boundaries, a layered block with a length of 55 m, whose two side nodes are restricted by the equal-displacement condition, is adjacent to the near-field ground to simulate the one-dimensional layered behavior of free ground in the far field. The boundary condition of the piles in the calculation is that the head of the pile is fixed with the footing and the toe of the pile is free. The boundary condition of the pier is that the bottom of the pier is fixed with the footing.

In modeling the bed rock, it is true that if the depth of bed rock is changed, the eigen-frequency of the whole ground will change and, correspondingly, the seismic response of the ground will be affected, as has been pointed out in many previous studies. In the present paper, because most of the attention is paid to the strong nonlinearity of the structure, for simplicity, only one depth was considered.

Fig. 14 shows the input earthquake wave used in the analysis, which is part of an earthquake wave predicted in the Nagoya area, with a maximum acceleration of 494 gal in the horizontal direction. A Rayleigh type of damping was adopted and the values of the ground and structures were assumed to be 2% and 10%, respectively, in the dynamic analysis of the full system. A direct integration method of Newmark-β was adopted in the dynamic analysis and the time interval of the integration was 0.0025 s. It should be point out that in the case of analyses considering strong nonlinearity, only the initial stiffness of the materials was used in the calculation of the Rayleigh damping.

Table 7
Material parameters of elastic beam for steel pier.

E_s (kPa)	A (m^2)	I_x (m^4)	I_y (m^4)	v	J (m^4)	γ (kN/m^3)
2.1*e*8	1.68*e*−2	9.77*e*−3	4.52*e*−3	0.25	1.43*e*−2	78.5

Table 9
Material parameters of nonlinear beam for steel pier.

E_{s0} (kPa)	E_t (kPa)	v	γ (kN/m^3)	σ_{y0} (kPa)	t (m)	h_m
2.1*e*8	2.1*e*6	0.25	78.5	2.0*e*5	2.36*e*−3	0.00

Table 8
Material parameters of trilinear beam for steel pier.

E_s (kPa)	A (m^2)	I_x (m^4)	I_y (m^4)	v	γ (kN/m^3)	$a1$	$a2$	M_c (kN m)	M_y (kN m)	M_u (kN m)
2.1*e*8	1.68*e*−2	9.77*e*−3	4.52*e*−3	0.25	78.5	0.1	0.001	1506	1642	6000

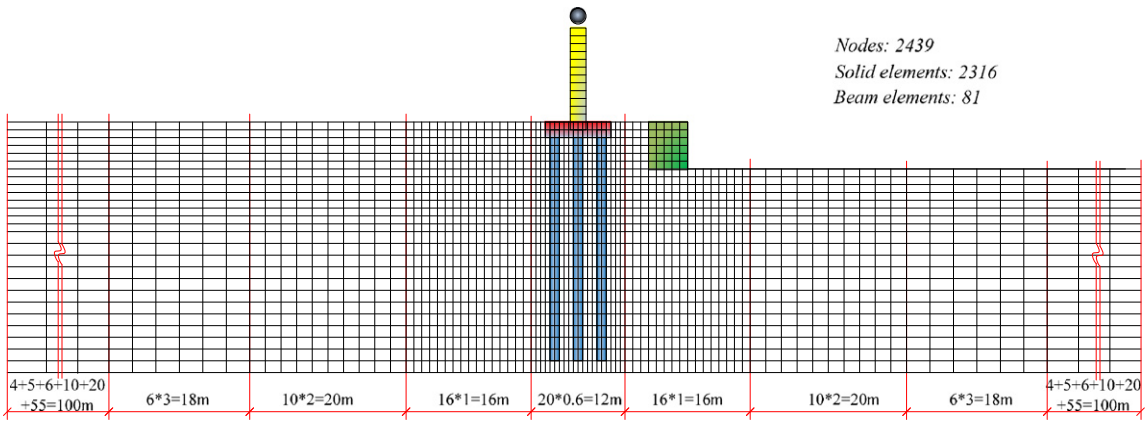

Fig. 13. Finite element mesh.

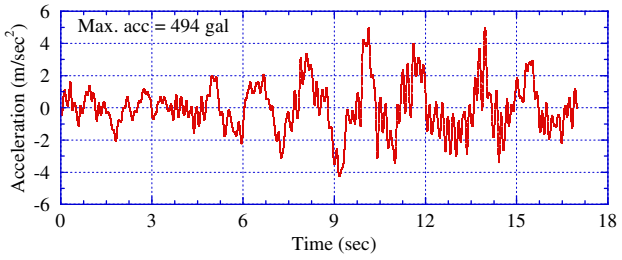

Fig. 14. Input earthquake wave.

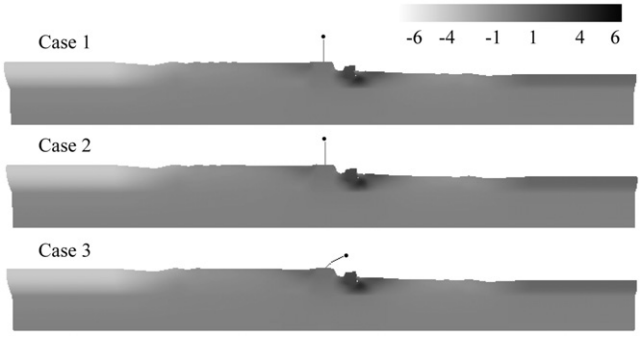

Fig. 15. Distribution of horizontal displacement (unit: m).

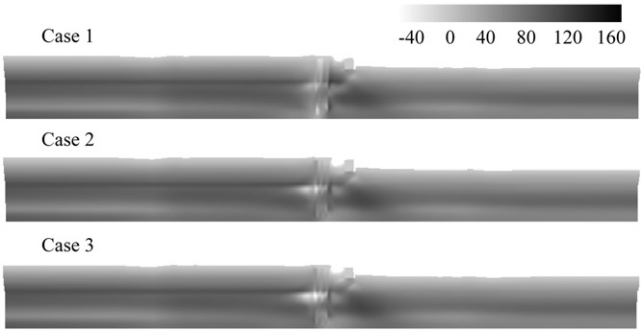

Fig. 16. Distribution of EPWP generated in soils at 10.25 s (unit: kPa).

3.1. *Influence of the nonlinearity of super structure described by different models on soil–structure interaction*

In order to investigate the influence of the nonlinearity of superstructure described by different models on soil–structure interaction, the analytical results obtained from the following 3 types of analyses are compared and discussed in detail:

Case 1: the pier is modeled by elastic linear beam elements based on infinitesimal deformation theory (hereafter referred to as the elastic model).
Case 2: the pier is modeled by trilinear beam elements based on infinitesimal deformation theory (hereafter referred to as the trilinear model).
Case 3: the pier is modeled by box thin-walled beam elements which can take both the material and geometrical nonlinearity into consideration (hereafter referred to as the nonlinear model).

Fig. 15 shows the distribution of horizontal displacement in three cases after the earthquake had finished. Fig. 16 shows the distribution of excess pore water pressure (EPWP) generated in the soils at 10.25 s for all cases. From these figures, it can be found that in the far field (30 m away from the footing) not only the deformation of the field, but also the EPWP generated in the soils was less affected by the nonlinearity of the pier. Therefore, more attention should be focused on the near field to investigate the influence of the nonlinearity of superstructure on the behavior of the soils and foundation. Here it should be noted that at 10.25 s, the values of EPWP in the sandy soils of the top two layers exceeded the initial effect stresses of those soils. Therefore, almost all of those soils had entered into the cyclic mobility state with finite deformation occurring. At the end of the earthquake, large residual deformation in the soils remained, as shown in Fig. 15.

Fig. 17 shows the comparison of the responding displacement and acceleration at the top and bottom of pier obtained from the aforementioned analyses. The responding displacements at the top of pier in the case of the nonlinear model were much larger than those of other

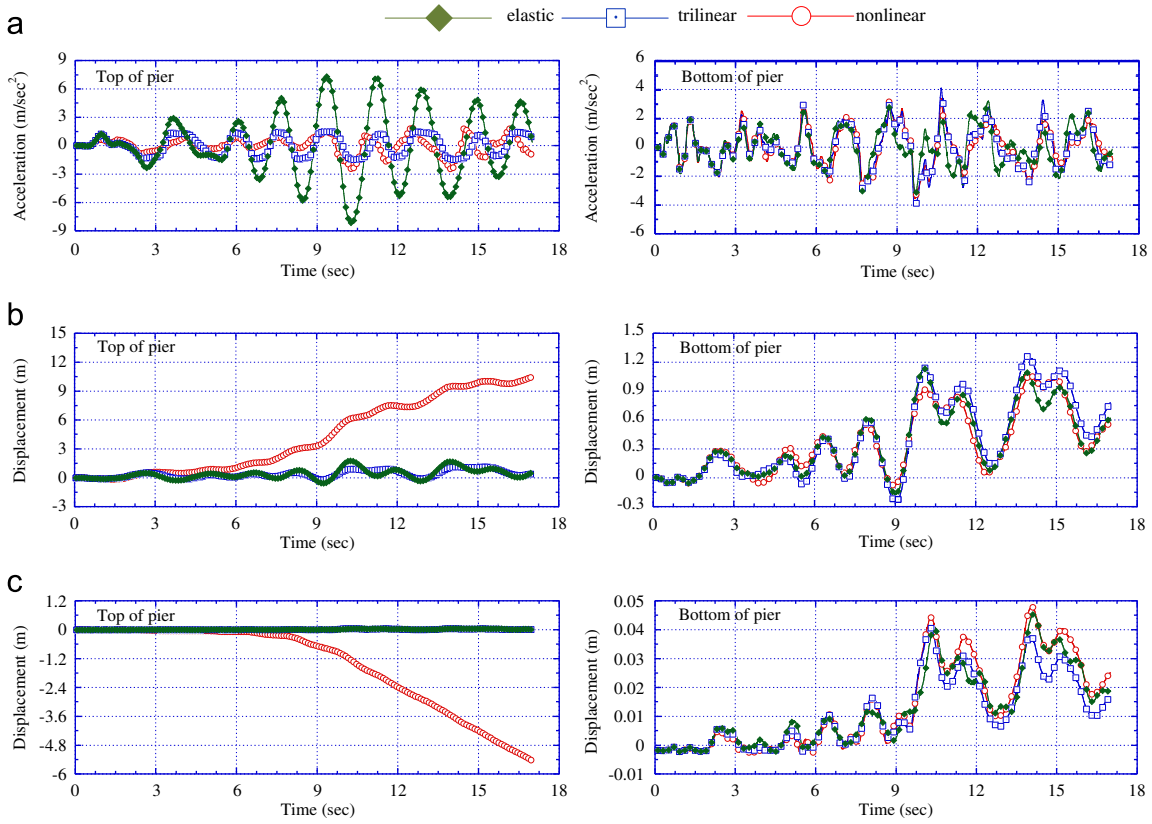

Fig. 17. Respond acceleration and displacement obtained from different analyses. (a) Responded acceleration, (b) responded horizontal displacement and (c) responded displacement in vertical direction.

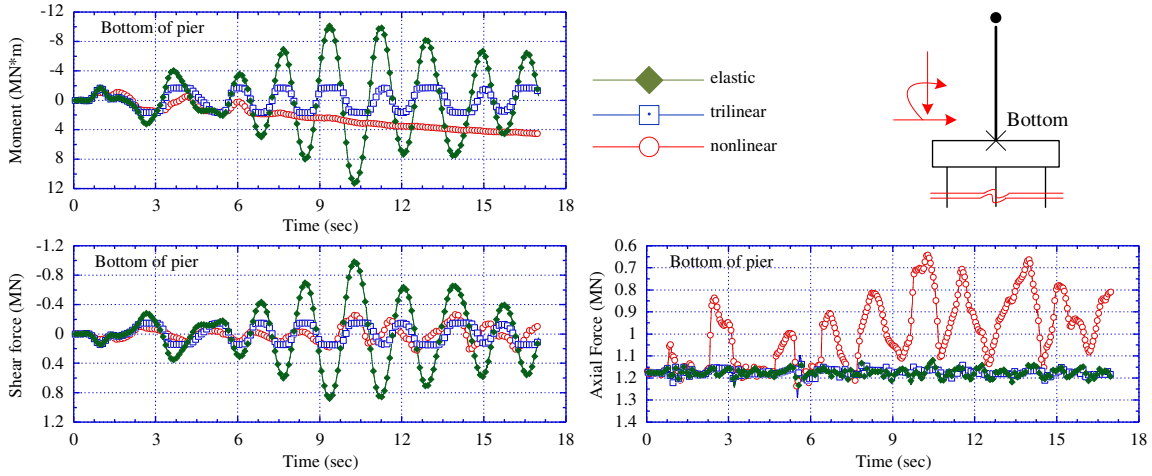

Fig. 18. Sectional forces at the bottom of pier.

cases. In the calculation, the maximum relative horizontal displacement between the top and bottom of the pier in the nonlinear case was about 9 m, but in other cases it did not exceed 0.5 m. This is because the beam elements for the pier used in the case of the elastic and trilinear model were based on infinitesimal deformation theory, and therefore do not have the ability to display large deformation. Meanwhile, the responding acceleration at the top of pier in the case of the elastic model was larger than in the other models. At the bottom of the pier, however, the responding acceleration and displacement history were almost the same shape for all three cases. Therefore, it can be deduced that the nonlinearity of the pier does not significantly influence the deformation of the ground, which is mainly dependent on the mechanical behavior of the soils.

Fig. 18 shows the sectional forces at the bottom of pier for all three cases. As mentioned above, in the case of the elastic model, because there was no energy absorption due to hysteresis attenuation, serious vibration occured and

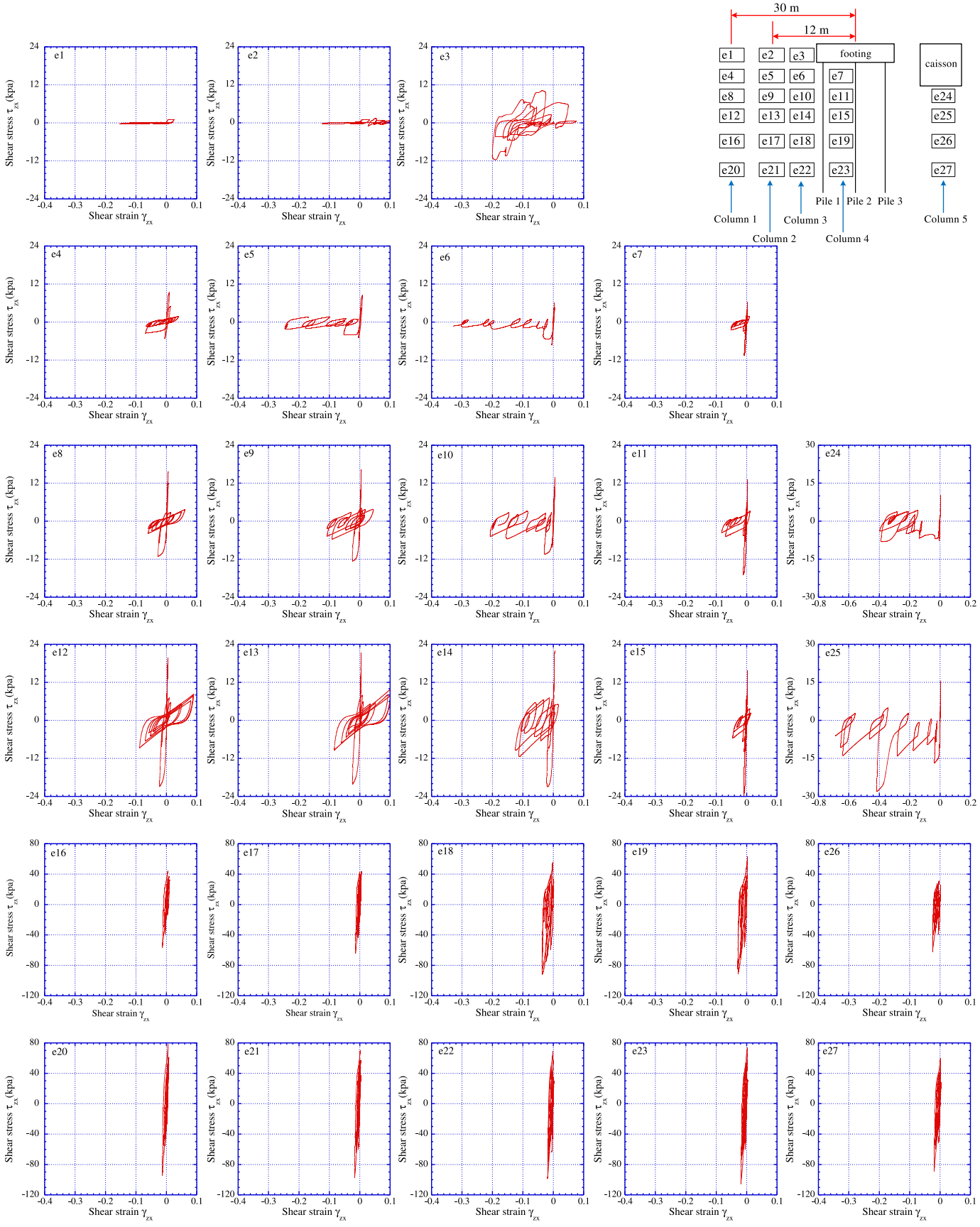

Fig. 19. Stress–strain relations of ground at different positions.

consequently the moment and the shear forces were much larger than those of the trilinear and the nonlinear models. Obviously, it was not possible for the models based on the infinitesimal deformation scheme to trace the large deformation of the superstructure in the earthquake process. In the calculation, the maximum moment acting on the bottom of the pier in the nonlinear model was 4.56 MN m, whereas the moment in the trilinear model was only 1.67 MN m. This notable difference can be expected to cause great different internal forces in the piles as described in the next section. Therefore, the nonlinearity of the superstructure must be taken into consideration in problems involved with soil–structure interaction when finite deformation occurs.

3.2. Dynamic behaviors of soils and RC piles in earthquake considering the nonlinearities of super structure

Fig. 19 shows the stress–strain relations of ground at different positions. On the left side of the footing, the shear strains of the soils in Column 3 are much larger than the others. The maximum shear strain at the interface of the soils and piles was about 0.34, while further afield (30 m away from the footing) it was less than 0.08. The hysteresis loops of the shear stress–strain relations of the soils in Column 3 are also much bigger than those at other places. It can be seen that the shear strains of the soils between the piles (soils in Column 4) were very small and almost the same as those further afield. Additionally, the stress–strain relations of the soils under the RC caisson (soils in Column 5) are also represented. Because soils near the caisson are most easy to liquefy, the deformation in this area was very large, with a maximum shear strain of 0.68.

Fig. 20 shows the histories of the mean effective stress and EPWP of the ground at different positions. From the figures, it can be seen that EPWP in the sandy soils increased quickly, and the effective stresses in those soils decreased almost to zero after about 5 s. Therefore, it is clear that the sandy soils display a notable phenomenon of liquefaction in the process of earthquake, whereas the clayed soils do not easily show this performance, as shown in Fig. 19.

Figs. 21–24 show the distribution of the sectional forces in the piles at the times of 9.02 s, 9.86 s, 13.79 s and 16.04 s, respectively, from the calculation with the nonlinear model. In these figures, the sectional forces M, S and N are normalized with M_{max}, S_{max} and N_{max} that represent the maximum values of the bending moment, the shear force and the axial force existed in all piles, respectively. Pile 1 was a front pile and Pile 3 was a back pile. At the time of 9.02 s, the different axial force occurring in Pile 1 to Pile 3, the distributions of the bending moments and the

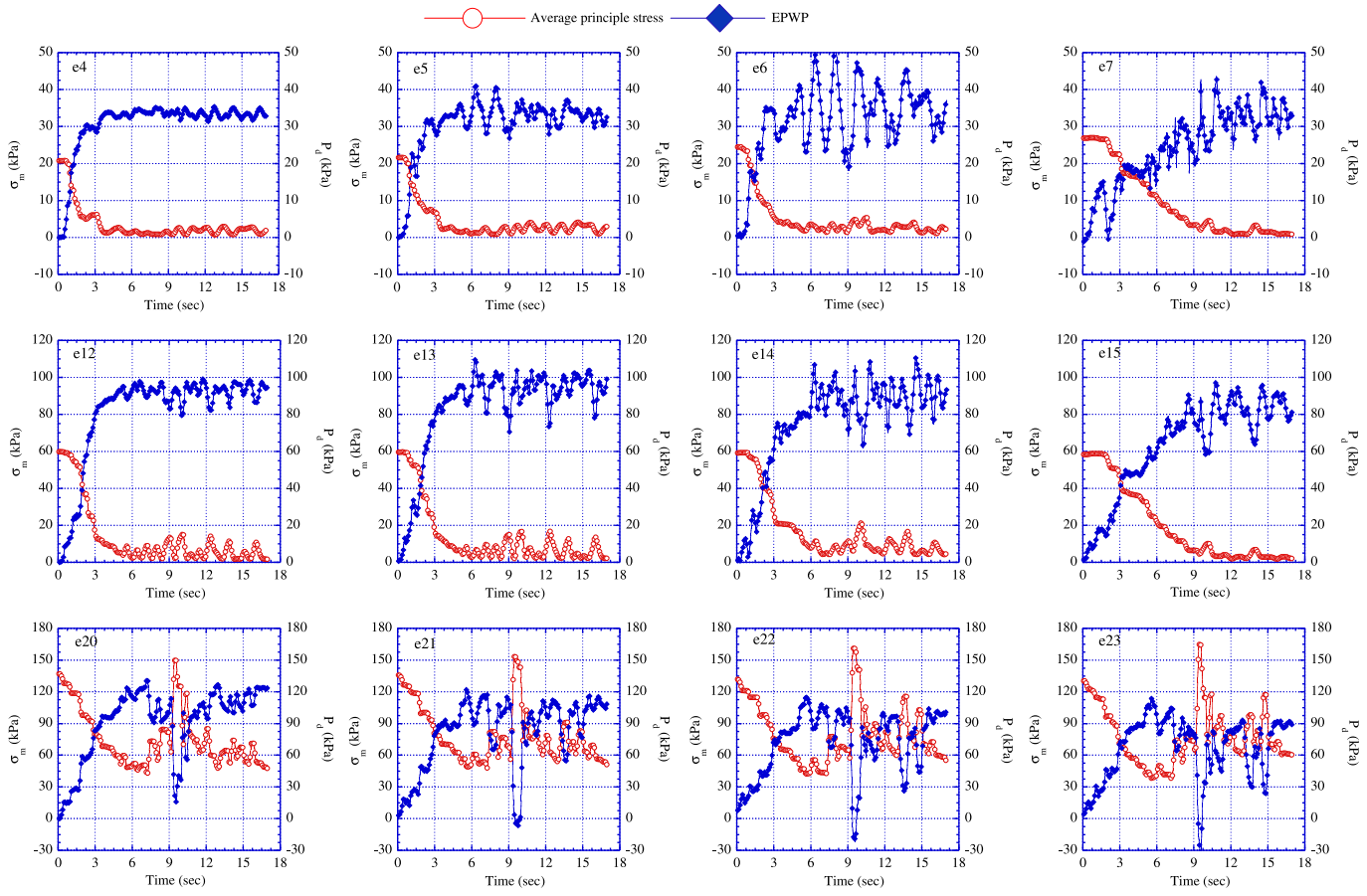

Fig. 20. Mean effective stress (σ_m) and EPWP (P_d) of ground at different positions.

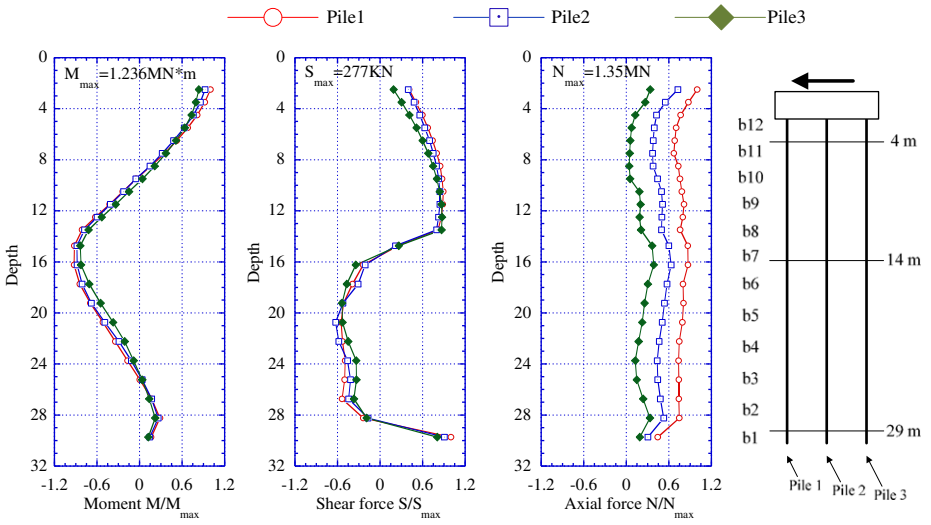

Fig. 21. Distribution of sectional forces of group piles (t=9.02 s).

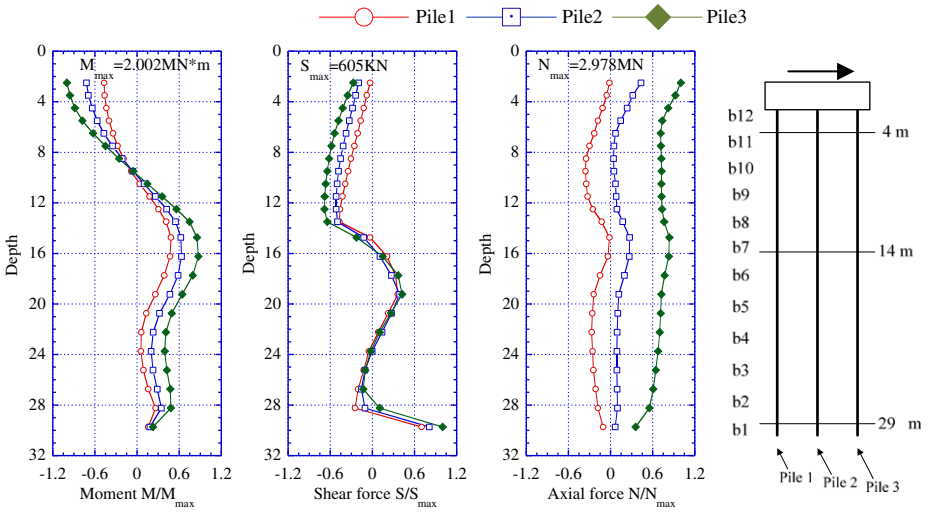

Fig. 22. Distribution of sectional forces of group piles (t=9.86 s).

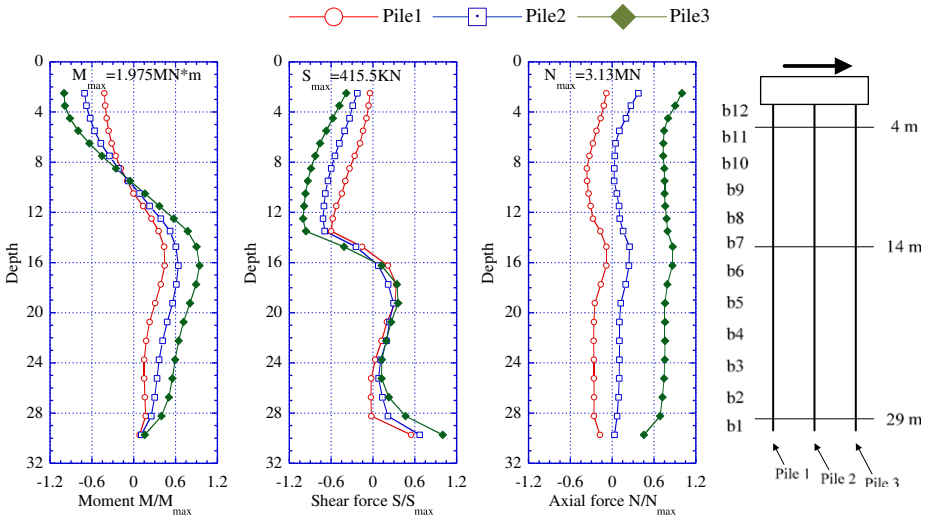

Fig. 23. Distribution of sectional forces of group piles (t=13.79 s).

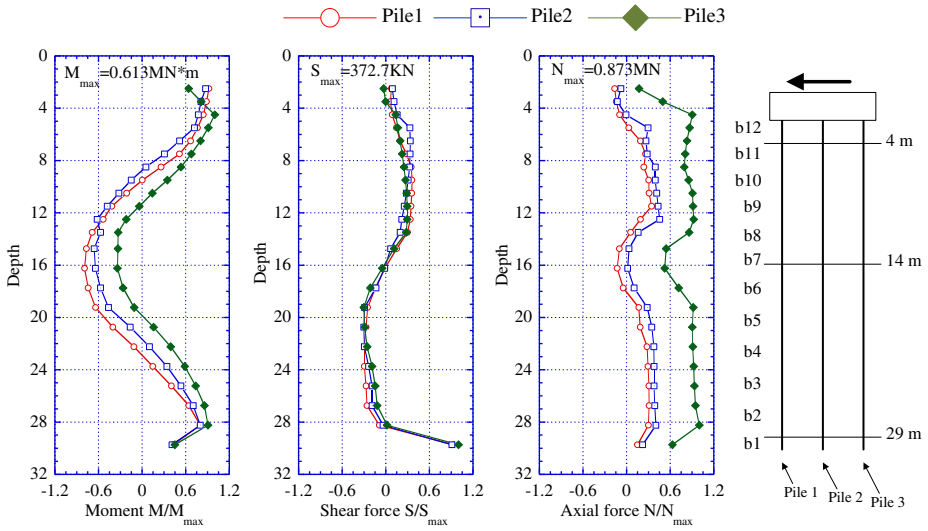

Fig. 24. Distribution of sectional forces of group piles ($t=16.04$ s).

shear forces in different piles was quite different. As described by Zhang and Kimura (2002), those differences show a very clear tendency: the larger the axial force, the larger the bending moment and the shear force. In this paper, by using AFD model to describe the piles, this phenomenon can be well identified. From these figures, it can be seen that, the difference of the axial forces in the piles depends on the ground vibration before large deformation of the pier happening, as shown at the times of 9.02 s and 9.86 s. When the deformation of the pier becomes extremely large, however, the moment of the nodal mass due to gravitation respected to the bottom of the pier becomes predominant, and this moment is hereafter referred to as extra moment. From then on, the axial force of Pile 3 is always larger than that of Pile 1, even if Pile 3 becomes a back pile, as shown at the times of 13.79 s and 16.04 s, due to the unrecoverable finite deformation.

Fig. 25 shows the histories of the moments in the piles at the corresponding positions. It is known that due to the plastic deformation of the pile, residual moments remain after the earthquake has finished. It can be seen that, as the earthquake vibration goes on, the difference of the moments among the piles increases remarkably. Because the times when the relatively large bending moment occur are 9.02 s, 9.86 s, 13.79 s and 16.04 s, it is reasonable to select the sectional forces at these times as the representatives compared in Figs. 21–24. It should be pointed out that at the same times, a relative large horizontal displacement occurred in the ground (this is not shown in the figure).

From Fig. 25, it can be seen that in the first six seconds, the difference of the moments and the shear forces of different piles was relatively insignificant even though the axial forces were quite different. This observation is rational and similar to the concepts in common design practice. The variations of axial forces apparent at different piles must be affected by original static loads and also the additional stresses due to the moments acting on top of the cap. It has been learned that the pile load distributions are only important in static cases and steady-state vibrations with relative smaller frequencies (Chang et al., 2009). In the finite deformation region, however, the above discussion is no longer valid because it can be seen from Figs. 22–25 that a large difference of the moments and the shear forces occurred in the different piles due to the consideration of the finite deformation.

In order to check the accuracy of the numerical simulation by DBLEAVES, a linear elastic analysis for an elevated bridge system was conducted and compared with the results obtained by ABAQUS. In this analysis, the full system consisted of a steel pier as the superstructure, a group-pile foundation and a ground composed of four layers, as shown in Fig. 26. The material parameters of the ground used in the analysis are listed in Table 10. The material parameters and the sizes of the piles, the foundation and the pier were the same as those in the model of the full system shown in Fig. 10.

In the eigen-mode analysis, a subspace iteration method was used and the dynamic analysis was conducted by the direct integration method of Newmark-β in which the time interval of the integration was 0.005 s. Fig. 27 shows the first five order modes of the full system. From the figures, we can find that the results calculated by the two programs coincide well with each other.

Fig. 28 shows the responding acceleration and displacement at the top of the pier obtained by the two programs. From the comparison, it is known that DBLEAVES has good accuracy for numerical simulations.

4. Conclusions

In this paper, a FEM-based numerical method considering the geometric and material nonlinearity of space frames, whose framework was established in structural

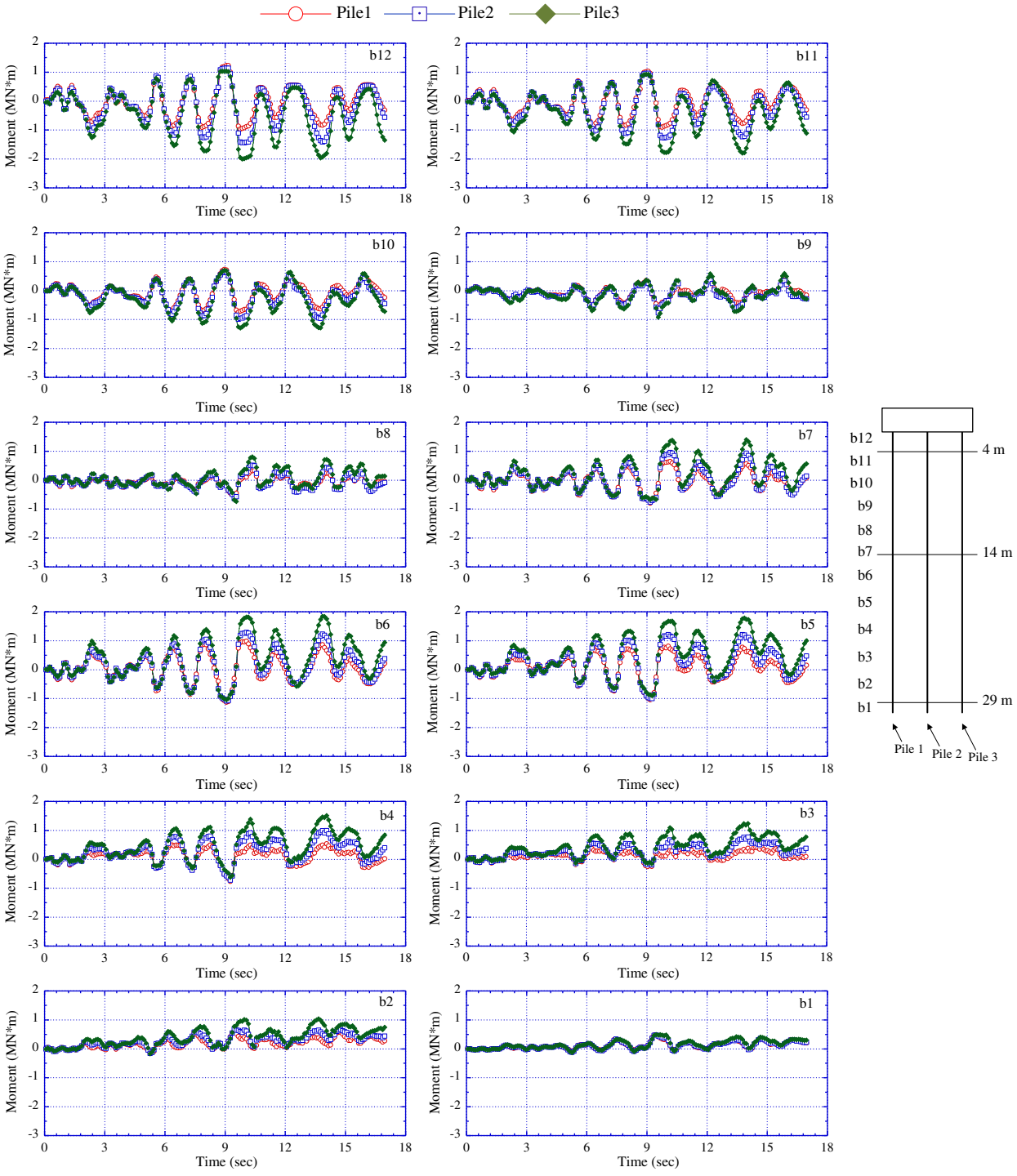

Fig. 25. Time history of bending moment of piles.

engineering (Li and Goto, 1998), was introduced into the FEM code known as DBLEAVES, a code which has mainly been used for numerical analyses in geotechnical engineering. By introducing this framework, it is possible to describe the nonlinear behavior in the finite deformation scheme, not only for geomaterials but also for structures. Throughout the presented work, the following conclusions can be made:

1. By using a co-rotational method, the geometric nonlinearity can be precisely considered in three-dimensional space, even when an extremely large rotation happens. The finite deformation can be described with the infinitesimal strain scheme together with rigid rotation in the finite element method. The procedure to derive the incremental stiffness equations for a beam element was simplified using the rotational components

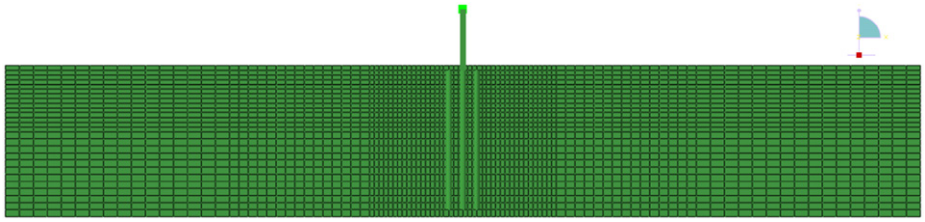

Fig. 26. FEM model of an elevated bridge for linear analyses.

Table 10
Material parameters of the ground used in linear elastic analysis.

No. of layers	E_s (kPa)	v	γ (kN/m^3)	Depth (m)
Soil1 (reclaimed sand)	5.0*e*3	0.3	18.0	4.0
Soil2 (alluvial sand)	1.0*e*4	0.3	18.0	10.0
Soil3 (alluvial clay)	2.0*e*4	0.4	18.0	15.0
Soil4 (diluvial gravel)	2.0*e*5	0.3	18.0	6.0

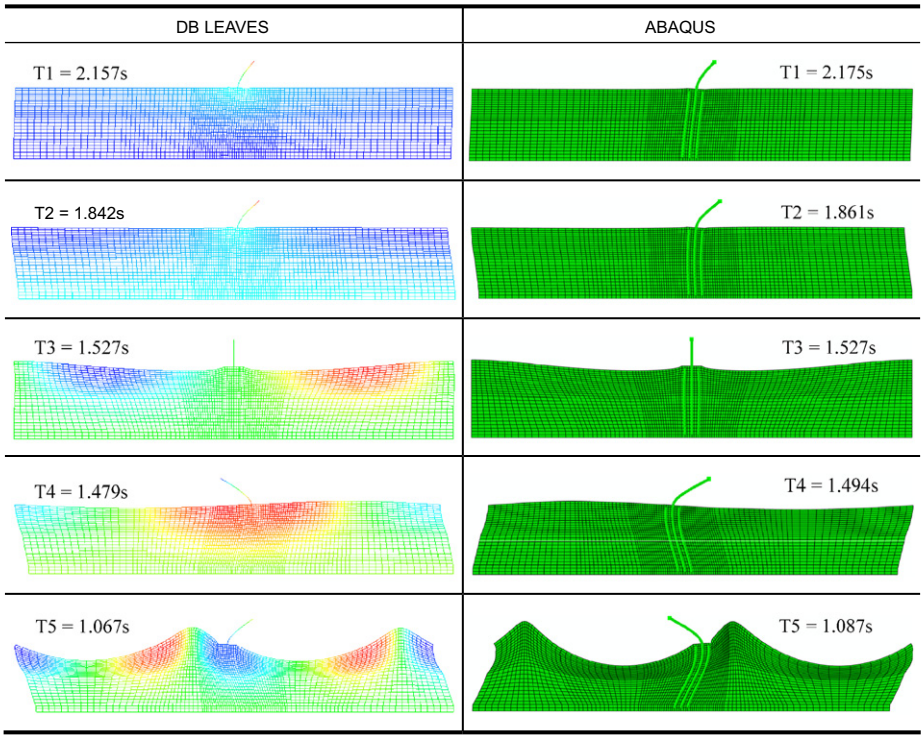

Fig. 27. First five modes of the full system.

around the co-rotational coordinates, which can be treated as vector quantities. As an example to show the accuracy of the presented calculation, a classical example was simulated, in which an initially-straight cantilever was subjected to an end moment at one end of the beam and was finally bent into complete circle. This result was exactly the same as that reported in the literature.

2. A mixed strain hardening bilinear model based on the Von Mises yield criterion was adopted to derive the elastoplastic stress–strain relationship. The effect of shear stresses due to transverse shear deformations and Saint-Venant torsional shear deformation was properly considered in the yield criterion. Based on the framework, it is easy to extend the stress–strain relation to any sophisticated or advanced constitutive law for structural materials if necessary.
3. A Timoshenko beam element with a thin-wall cross section was introduced, which has the ability to deal with the analysis of the column or beam with a small length-section ratio, in which the effect of both the transverse shear deformation due to bending and the

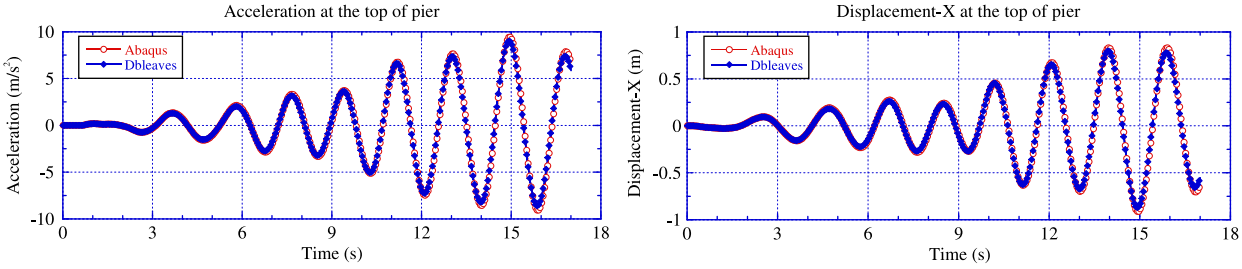

Fig. 28. Responding acceleration and displacement at the top of pier.

torsional shear deformation can be considered in the analysis.

4. By introducing a beam element which can take into consideration the material and geometric nonlinearity of superstructure, any large deformation of the superstructure can be traced in the process of earthquake action. It was shown that, because of the large deformation of the superstructure due to earthquake motion, the extra moment of superstructure at the bottom of pier becomes remarkable, and this can only be simulated properly with the proposed numerical method. It is obvious that without adopting the finite deformation scheme for the superstructure, it is impossible to describe the extra moment.
5. As the result of proper description for the extra moment occurred in the superstructure, the external forces acting on the piles from the superstructure were able to be evaluated more precisely. Moreover, by using the AFD model, which can well simulate the axial-force dependency of RC materials under monotonic and cyclic loading, the difference of the sectional forces among the front, back and middle piles in a group-pile foundation subjected to seismic loading can be well simulated.
6. The cyclic mobility model was adopted to describe the behavior of ground subjected to seismic loading. The Jaumann rate strain tensor was used in the cyclic mobility model to deal with the finite deformation of soils. In the simulation, the EPWP in sandy soils increased very quickly and the soils entered into the cyclic mobility state with large deformation occurring. The clayed soils, as expected, did not show this behavior. The soils near to the group-pile foundation showed very large shear strain compared with the soils in other areas. The soils more far afield, however, were less influenced by the soil–structure interaction.
7. In the calculation, due to the consideration of the finite deformation, the maximum moment acting on the bottom of the pier was almost three times larger than that in the calculation using the infinitesimal-strain scheme. Consequently, this notable difference will result in a great difference in the sectional forces in the piles. Therefore, the nonlinearity of the superstructure must be taken into consideration for problems involving soil–structure interactions when finite deformation occurs.
8. Therefore, for the problems involving soil–structure interaction encountered in geotechnical engineering, a full system consisting of the ground, the foundation and the superstructure should be modeled. Moreover, both the material and geometric nonlinearities of the soils and the structures should be taken into consideration by introducing proper constitutive models and finite deformation schemes.
9. By properly introducing the structural elements that can deal with both the geometric and the material nonlinearities of the structures into geotechnical engineering, the accuracy of FEM analysis in geotechnical engineering will be improved significantly, especially for problems related to soil–structure interaction, and the accuracy of FEM simulations in geotechnical engineering may be accepted by structural engineering. The presented method provides us with a tool to realize this ultimate goal.

Acknowledgment

The authors would like to give their gratitude to Prof. Yoshiaki GOTO of the Nagoya Institute of Technology, for his valuable suggestions and comments.

Appendix

The transformation matrix $[R]$ is given in detail as follow:

$$[R]=\begin{bmatrix} -[R_G] & [Et_1] & [R_G] & [Et_1] \\ [0] & -[DR_1][BR(\theta_1,\phi_1)]^{-1}[R_1] & [0] & -[DR_2][BR(\theta_2,\phi_2)]^{-1}[R_2] \end{bmatrix} \tag{A1}$$

where $(\phi_i,\theta_i,\psi_i)\quad (i=1,\ 2)$ are Eulerian angles.

$$[R_i]=[TR(\phi_i,\theta_i,\psi_i)]\quad (i=1,\ 2) \tag{A2}$$

$$[R_G]=[TR(\overline{\phi},\overline{\theta},\overline{\psi})] \tag{A3}$$

where

$\overline{\phi}=((\phi_1+\phi_2/2)/2),\ \overline{\theta}=(\theta_1+\theta_2)/2,\quad \overline{\psi}=(\psi_1+\psi_2)/2$

$$[TR(a,b,c)]=\begin{bmatrix}1&0&0\\0&\cos a&\sin a\\0&-\sin a&\cos a\end{bmatrix}\begin{bmatrix}\cos b&0&-\sin b\\0&1&0\\\sin b&0&\cos b\end{bmatrix}\times\begin{bmatrix}\cos c&\sin c&0\\-\sin c&\cos c&0\\0&0&1\end{bmatrix}\tag{A4}$$

$$[BR(a,b)]=\begin{bmatrix}1&0&-\sin a\\0&\cos b&\cos a\sin b\\0&-\sin b&\cos a\cos b\end{bmatrix}\tag{A5}$$

$$[DR_1]=\begin{bmatrix}1/2&(\psi_2-\psi_1)\cos\overline{\theta}/4&-\sin\overline{\theta}/2\\-(\psi_2-\psi_1)\cos\overline{\theta}\cos\overline{\phi}/4+(\theta_2-\theta_1)\sin\overline{\varphi}/4&(\psi_2-\psi_1)\sin\overline{\theta}\sin\overline{\phi}/4+\cos\overline{\phi}/2&\cos\overline{\theta}\sin\overline{\phi}/2\\(\psi_2-\psi_1)\cos\overline{\theta}\sin\overline{\phi}/4+(\theta_2-\theta_1)\cos\overline{\phi}/4&(\psi_2-\psi_1)\sin\overline{\theta}\cos\overline{\phi}/4-\sin\overline{\phi}/2&\cos\overline{\theta}\cos\overline{\phi}/2\end{bmatrix}\tag{A6}$$

$$[DR_2]=\begin{bmatrix}-1/2&(\psi_2-\psi_1)\cos\overline{\theta}/4&\sin\overline{\theta}/2\\-(\psi_2-\psi_1)\cos\overline{\theta}\cos\overline{\phi}/4+(\theta_2-\theta_1)\sin\overline{\phi}/4&(\psi_2-\psi_1)\sin\overline{\theta}\sin\overline{\phi}/4-\cos\overline{\phi}/2&-\cos\overline{\theta}\sin\overline{\phi}/2\\(\psi_2-\psi_1)\cos\overline{\theta}\sin\overline{\phi}/4+(\theta_2-\theta_1)\cos\overline{\phi}/4&(\psi_2-\psi_1)\sin\overline{\theta}\cos\overline{\phi}/4+\sin\overline{\phi}/2&-\cos\overline{\theta}\cos\overline{\phi}/2\end{bmatrix}\tag{A7}$$

$$[Et_1]=\tfrac{1}{2}[E][D]\left[BR(\overline{\theta},\overline{\phi})\right][BR(\theta_1,\phi_1)]^{-1}[R_1]\tag{A8}$$

$$[Et_2]=\tfrac{1}{2}[E][D]\left[BR(\overline{\theta},\overline{\phi})\right][BR(\theta_2,\phi_2)]^{-1}[R_2]\tag{A9}$$

$$[D]=\begin{bmatrix}u_2-u_1&0&0\\v_2-v_1&0&0\\w_2-w_1+l&0&0\\0&u_2-u_1&0\\0&v_2-v_1&0\\0&w_2-w_1+l&0\\0&0&u_2-u_1\\0&0&v_2-v_1\\0&0&w_2-w_1+l\end{bmatrix}\tag{A10}$$

$$[E]=\begin{bmatrix}0&0&0&-c_1&-c_2&-c_3&b_1&b_2&b_3\\c_1&c_2&c_3&0&0&0&-a_1&-a_2&-a_3\\-b_1&-b_2&-b_3&a_1&a_2&a_3&0&0&0\end{bmatrix}\tag{A11}$$

where

$a_1=\cos\overline{\theta}\cos\overline{\psi};\quad a_2=\cos\overline{\theta}\sin\overline{\psi};\quad a_3=-\sin\overline{\theta};$

$b_1=-\cos\overline{\varphi}\sin\overline{\psi}+\sin\overline{\varphi}\sin\overline{\theta}\cos\overline{\psi};$

$b_2=\cos\overline{\varphi}\cos\overline{\psi}+\sin\overline{\varphi}\sin\overline{\theta}\sin\overline{\psi};$

$b_3=\sin\overline{\varphi}\cos\overline{\theta};$

$c_1=\sin\overline{\varphi}\sin\overline{\psi}+\cos\overline{\varphi}\sin\overline{\theta}\cos\overline{\psi};$

$c_2=-\sin\overline{\varphi}\cos\overline{\psi}+\cos\overline{\varphi}\sin\overline{\theta}\sin\overline{\psi};$

$c_3=\cos\overline{\varphi}\cos\overline{\theta}\tag{A12}$

References

Abaqus, 2008. ABAQUS/CAE: user's manual, version 6.8. ABAQUS Inc., USA.

Asaoka, A., Nakano, M., Noda, T., 1994. Soil–water coupled behavior of saturated clay near/at critical state. Soils and Foundations 37 (l), 91–105.

Asaoka, A., Nakano, M., Noda, T., 1998. Super loading yield surface concept for the saturated structured soils. In: Proceedings of the Fourth European Conference on Numerical Methods in Geotechnical Engineering—NUMGE98, pp. 232–242.

Chang, D.W., Lin, B.S., Cheng, S.H., 2009. Lateral load distributions on grouped piles from dynamic pile-to-pile interaction factors. International Journal for Numerical and Analytical Methods in Geomechanics 33 (2), 173–191.

Goto, Y., Li, X.S., Kasugai, T., Obata, M., 1995. Analysis of Greenhill problem by a co-rotational method. Journal of Structural Engineering 41A, 411–420.

Hashiguchi, K., Ueno, M., 1977. Elastoplastic constitutive laws of granular material, constitutive equations of soils. In: Murayama, S., Schofield, A.N. (Eds.), Proceedings of the Ninth International Conference on Soil Mechanics and Foundation Engineering, Special Session 9. JSSMFE, Tokyo, pp. 73–82.

Hsiao, K.M., Horng, H.J., Chen, Y.R., 1987. A co-rotational procedure that handles large rotations of spatial beam structures. Computers and Structures 27 (6), 769–781.

Jin, Y., Bao, X.H., Kondo, Y., Zhang, F., 2010a. Numerical evaluation of group-pile foundation subjected to cyclic horizontal load. Frontiers of Architecture and Civil Engineering in China 4 (2), 196–207.

Jin, Y., Ye, B., Zhang, F., 2010b. Numerical simulation of sand subjected to cyclic load under undrained conventional triaxial test. Soils and Foundations 50 (2), 177–194.

Li, X.S., 1997. A Rigorous Numerical Method for Analysis of Geometric and Material Nonlinear Dynamic Behavior of Space Frames. Doctoral Dissertation. Nagoya Institute of Technology.

Li, X.S., Goto, Y., 1998. A three-dimensional nonlinear seismic analysis of frames considering panel zone deformations. Journal of Structural Engineering and Earthquake Engineering 15 (2), 201–213.

Noda, T., Asaoka, A., Nakano, M., 2008. Soil–water coupled finite deformation analysis based on a rate-type equation of motion incorporating the SYS Cam-clay model. Soils and Foundations 48 (6), 771–790.

Oka, F., 1992. A cyclic elasto-viscoplastic constitutive model for clay based on the non-linear hardening rule. In: Proceedings of Fourth International Symposium on Numerical Models in Geomechanics. Swansea, pp. 105–114.

Oka, F., Yashima, A., Kato, M., Sekiguchi, K., 1992. A constitutive model for sand based on the non-linear kinematic hardening rule and its application. In: Proceedings of the Tenth World Conference on Earthquake Engineering, vol. 5. Balkema, Madrid, pp. 2529–2534.

Oka, F., Yashima, A., Shibata, T., Kato, M., Uzuoka, R., 1994. FEM–FDM coupled liquefaction analysis of a porous soil using an elasto-plastic model. Applied Scientific Research 52, 209–245.

Oka, F., Yashima, A., Tateishi, A., Taguchi, Y., Yamashita, S., 1999. A cyclic elastoplastic constitutive model for sand considering a plastic-strain dependence of the shear modulus. Geotechnique 49 (5), 661–680.

Sekiguchi, H., 1977. Rheological characteristics of clays. In: Proceedings of the Ninth International Conference on Soil Mechanics and Foundation Engineering, vol. 1. Tokyo, pp. 289–292.

Simo, J.C., Vu-Quoc, L., 1986. A three-dimensional finite strain rod model. Part II: Computational Aspects. Computer Methods in Applied Mechanics and Engineering 58, 79–116.

Wang, Q.Y., 1997. Strength Deterioration and Localization of Plastic Buckling Patterns of Plated Structures under Cyclic Loading. Doctoral Dissertation. Nagoya Institute of Technology.

Xia, Z.F., Ye, G.L., Wang, J.H., Ye, B., Zhang, F., 2010. Fully coupled numerical analysis of repeated shake-consolidation process of earth embankment on liquefiable foundation. International Journal of Soil Dynamics and Earthquake Engineering 30 (11), 1309–1318.

Yao, Y.P., Sun, D.A., Matsuoka, H., 2008. A unified constitutive model for both clay and sand with hardening parameter independent on stress path. Computers and Geotechnics 35 (2), 210–222.

Yashima, A., Oka, F., Shibata, T., Uzuoka, R., 1991. Liquefaction analysis by LIQCA. In: Proceedings of JGS Conference on Liquefaction of Ground and its Counter measure, pp. 165–174 (in Japanese).

Ye, B., Ye, G., Zhang, F., Yashima, A., 2007. Experiment and numerical simulation of repeated liquefaction–consolidation of sand. Soils and Foundations 47 (3), 547–558.

Ye, B., 2007. Experiment and Numerical Simulation of Repeated Liquefaction–Consolidation of Sand. Doctoral Dissertation. Gifu University.

Ye, G.L., 2011. DBLEAVES: user's manual, version 1.6, China. Shanghai Jaotong University (in Japanese and Chinese).

Zhang, F., Kimura, M., 2002. Numerical prediction of the dynamic behaviors of an RC group-pile foundation. Soil and Foundation 42 (3), 77–92.

Zhang, F., Kimura, M., Nakai, T., Hoshikawa, T., 2000. Mechanical behavior of pile foundation subjected to cyclic lateral loading up to the ultimate state. Soil and Foundation 40 (5), 1–18.

Zhang, F., Ye, B., Noda, T., Nakano, M., Nakai, K., 2007. Explanation of cyclic mobility of soils: approach by stress-induced anisotropy. Soils and Foundations 47 (4), 635–648.

Zhang, F., Jin, Y., Ye, B., 2010. A try to give a unified description of Toyoura sand. Soils and Foundations 50 (3), 679–693.

Zhang, F., Ye, B., Ye, G.L., 2011. Unified description of sand behavior. Frontiers of Architecture and Civil Engineering in China 5 (2), 121–150.